

Large eddy simulation of blockage effects in the assessment of wind effects on tall buildings

Yang Gao^a, Ming Gu^{*}, Yong Quan and Chengdong Feng

State Key Laboratory for Disaster Reduction in Civil Engineering, Tongji University, P.O. Box 200092, Shanghai, PR China

(Received October 5, 2019, Revised January 4, 2020, Accepted February 20, 2020)

Abstract. The blockage effect on the aerodynamic characteristics of tall buildings is a fundamental issue in wind tunnel test but has rarely been addressed. To evaluate the blockage effects on the aerodynamic forces on a square tall building and flow field peripherally, large eddy simulations (LES) were performed on a 3D square cylinder with an aspect ratio of 6:1 under the uniform smooth inflow and turbulent atmospheric boundary layer (ABL) inflow generated by the narrowband synthesis random flow generator (NSRFG). First, a basic case at a blockage ratio (BR) of 0.8% was conducted to validate the adopted numerical methodology. Subsequently, simulations were systematically performed at 6 different BRs. The simulation results were compared in detail to illustrate the differences induced by the blockage, and the mechanism of the blockage effects under turbulent inflow was emphatically analysed. The results reveal that the pressure coefficients, the aerodynamic forces, and the Strouhal number increase monotonically with BRs. Additionally, the increase of BR leads to more coherence of the turbulent structures and the higher intensity of the vortices in the vicinity of the building. Moreover, the blockage effects on the aerodynamic forces and flow field are more significant under smooth inflow than those under turbulent inflow.

Keywords: blockage effect; large eddy simulation; tall building; aerodynamic forces; flow field

1. Introduction

In recent years, with the new generation of high-rise buildings, wind loads have become the main governing load of structural design, and have a substantial impact on both the structural integrity and the serviceability of the building (Irwin 2009). Wind tunnel testing, as one of the most important approaches for the assessment of wind loads on buildings, has been shown to be a suitable and reliable technique by numerous studies and applications (Cermak 2003, Irwin 2009, Cochran and Derickson 2011). Generally, when wind tunnel experiments are carried out, models need to be mounted in the channel at a reduced scale. To obtain accurate measurements with certain geometric and dynamic similarity, the model should satisfy the requirement of a smaller scale dimension. Frequently, such a building model is sufficiently large to result in appreciable constraining effects due to the tunnel walls, namely the blockage effect. It is well known that the flow will be accelerated when it passes the reduced cross-section near the building to satisfy the continuity requirement (solid blockage), and the wake velocity and the vortex shedding from the model will be modified as a result of the confinement of the tunnel walls (wake blockage). Thus, the flow patterns and wind forces produced in the wind tunnel will be much different from those obtained in the unbounded nature environment.

Therefore, the blockage effects on the aerodynamic characteristics of tall buildings have always been a fundamental issue to be addressed in wind tunnel testing (Raju and Singh 1975, Utsunomiya *et al.* 1993).

In the past, many investigations concerning the effects of blockage have been carried out using the wind tunnel technique. Most of those studies were performed on flow past a two-dimensional rectangular cylinder where the cylinder is placed at the center of the channel (Courchesne and Laneville 1979, Petty 1979, Awbi 1983, Laneville 1990, Okajima *et al.* 1997, Reyes *et al.* 2013), and the variation in aerodynamic characteristics with respect to the blockage ratio (BR, which is defined as the ratio of the windward area of the model to the cross-sectional area of the wind tunnel), such as wind pressure distributions, drag coefficients, lift coefficients and the Strouhal number, have been extensively investigated. Additionally, several correction methods have been developed and widely used to correct test results of two-dimensional bluff bodies (Maskell 1963, Ramamurthy *et al.* 1989, Hackett and Cooper 2001). However, there are obvious differences between the flow features around the two-dimensional bluff bodies and three-dimensional buildings. For instance, as reported by Martinuzzi and Tropea (1993), the flow features such as horseshoe vortex in the front of the model, separation vortices at the sharp edges of the model on the roof and side walls, and arch vortex originating from the ground behind the model, are observed around a surface-mounted cube, which are much different from the flow field around the two-dimensional bluff bodies.

The research by Huang *et al.* (2007) shows that the incident wind velocity and turbulence intensity profiles have significant effects on both mean and fluctuating wind

*Corresponding author, Professor

E-mail: minggu@tongji.edu.cn

^aPh.D. Student

E-mail: 1410239@tongji.edu.cn

forces. However, systematic investigations of the blockage effects on the aerodynamic forces of a high-rise building have rarely been conducted by the experimental method, especially when the impact of atmospheric boundary layer (ABL) flow is also considered. When the wind tunnel test method is used to investigate this issue, a series of models with different geometric scales are needed to obtain different BRs. To ensure the comparability of the experimental results from different models, the incoming wind velocity profile and turbulence intensity profile must have the same distributions but different geometric scales as the corresponding models. Otherwise, when the measured results from several test cases with different inflow characteristics are compared, the differences due to the inflow will seriously affect the study of the blockage effect. However, for the ABL flow, achieving exactly the same wind velocity profile and turbulence intensity profile but different geometric scales are certainly difficult. Moreover, exploring the mechanism is one important topic in the research of the blockage effect. Indeed, the mechanism of the blockage effects on high-rise buildings under the ABL flow has rarely been studied. For this purpose, it is necessary to study the effects of blockage on the flow field around buildings. However, it is very complicated and difficult to obtain the flow field information in wind tunnel tests. It is encouraging that a useful approach to overcome these difficulties is to adopt the numerical technique of computational fluid dynamics (CFD).

As introduced by Blocken (2014) and Ricci *et al.* (2018), numerical approaches have several advantages compared to wind tunnel tests, such as lower costs, whole flow field data, well-controlled conditions, and no similarity constraints. Over the past few decades, with advancements in computer technology and improvements in the turbulence model and numerical methods (Tamura 2008), the CFD technique has been shown to have great reliability in numerous studies and has become a complementary tool to investigate wind flow around buildings (Blocken 2014, 2015, Thordal *et al.* 2019). In some respects, numerical simulations allow the study of phenomena that might be difficult to analyse in wind tunnel tests.

Many two-dimensional numerical investigations (Davis *et al.* 1984, Okajima *et al.* 1997) have been performed to study the wall confinement on the aerodynamic characteristics of a square cylinder. The results of these investigations show that the presence of the confining wall leads to an increase in drag, and the strength of the vortices shed from the cylinder is enhanced, which corresponds to an increase in the Strouhal number. The flow characteristics also change significantly with an increase in the BR. It should be noted that most of the numerical studies mentioned above involved solving the two-dimensional Navier-Stokes equation and were restricted to a low Reynolds number ($Re < 1000$). Kim *et al.* (2004) performed a large eddy simulation (LES) to simulate the flow field past a square cylinder in the physical configuration equivalent to that of the experiment carried out by Nakagawa *et al.* (1999). The BR used in their experiment and simulation is 20%, and the Reynolds number is 3000. Nevertheless, these simulations focus only on the flow

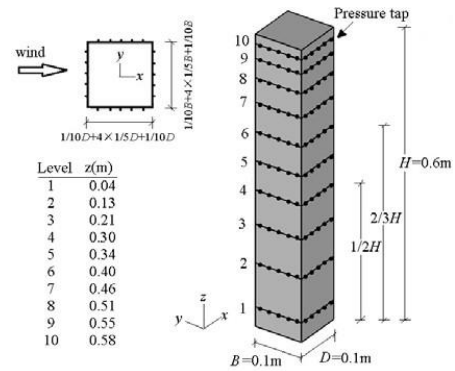


Fig. 1 Geometry of the high-rise building and pressure tap locations

around two-dimensional bluff bodies, and both the simulation model and the inflow boundary are far from the numerical simulation of the three-dimensional high-rise building because the nature of the flow field around the three-dimensional model is highly complex with impingement, separation and vortex shedding (Murakami 1998).

To sum up, numerical research on the blockage effect on the three-dimensional high-rise building has rarely been published to the best knowledge of the authors, although plenty of studies on LESs of high-rise buildings have been conducted. Therefore, the present study attempts to investigate the blockage effects in the assessment of wind effects on a typical square tall building via LES. In particular, two kinds of inlet boundary conditions are considered here, one is the turbulent ABL flow generated by the narrowband synthesis random flow generator (NSRFG) (Yu *et al.* 2018) technique and the other is uniform smooth inflow. First, numerical simulations in empty computational domains at $BR=0.8\%$ are iteratively performed by adjusting the inflow boundary condition generated by NSRFG until the desired wind fields are formed at the target locations. Then, numerical simulations of wind effects on a square tall building model at $BR=0.8\%$ are performed using the adjusted inflow boundary conditions. The performance of the numerical method is assessed through comparisons with available experimental results (Zheng *et al.* 2012). Subsequently, numerical simulations of wind effects on the same square tall building model but at the other 5 BRs are performed with the same procedure as the case at $BR = 0.8\%$. Moreover, simulations at all the 6 BRs are performed under the uniform smooth inflow. Finally, the simulation results are compared in detail to illustrate the difference in wind loads and flow fields due to the wall confinement, and the mechanism of the blockage effect is investigated.

2. Experimental setup

In this section, the experimental setup adopted to obtain pressure data used for comparison with LES results is described. The wind tunnel experiment (Zheng *et al.* 2012) was carried out at the TJ-2 boundary layer wind tunnel of Tongji University. The TJ-2 wind tunnel offers a test section

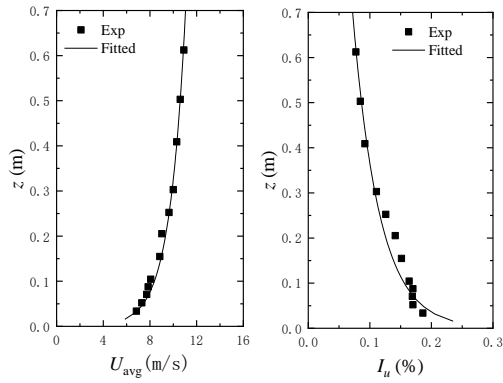


Fig. 2 Mean velocity and turbulence intensity profiles in the experiment

Table 1 Simulation cases and computational domain dimensions

Case	BR (%)	X direction	Y direction	Z direction	Inlet Conditions
1	0.8	90B	30B	25B	Turbulent / Smooth
2	2.5	90B	16.8B	14B	Turbulent / Smooth
3	5	90B	12B	10B	Turbulent / Smooth
4	7.8	90B	9.6B	8B	Turbulent / Smooth
5	10	90B	6B	10B	Turbulent / Smooth
6	15	90B	4B	10B	Turbulent / Smooth

with a 3.0 m width and a 2.5 m height. The experiment focuses on an isolated square high-rise building characterized by a width (B), depth (D) and height (H) ratio of $B:D:H=1:1:6$. The length scale was equal to $1/500$, leading to a model with $B=D=100$ mm and $H=600$ mm, as shown in Fig. 1. The high-frequency pressure integration (HFPI) method was used to characterize the wind loads on the building. The model was equipped with 200 pressure taps that acquired data synchronously at a sampling frequency of 312.5 Hz. The profiles of the mean velocity and streamwise turbulence intensity measured in the wind tunnel test are shown in Fig. 2, which is the target wind field characteristic for the LES cases under the turbulent inflow.

3. Large eddy simulation models

3.1 Computational domain and mesh schemes

Table 1 shows the computational cases with different domain dimensions but with the same square building model, resulting in 6 different BRs of 0.8%, 2.5%, 5%, 7.8%, 10%, and 15%. The model scale chosen for the present simulations is the same as that adopted in the wind tunnel experiment (Zheng *et al.* 2012), which was $\lambda_L = 1:500$.

First, the Case 1 simulation was performed as the baseline case. The computational domain size is $30B \times 25B$

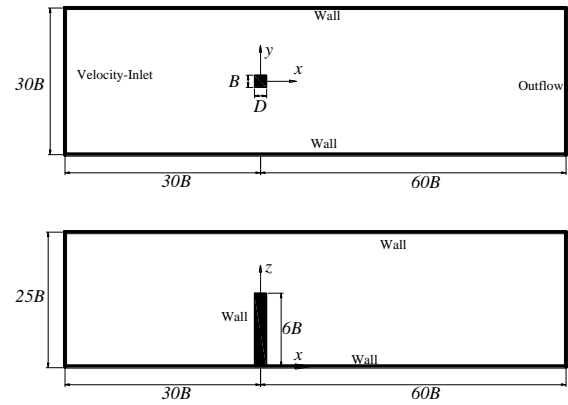


Fig. 3 Computational domain dimensions and boundary conditions for Case 1

$\times 90B$, as shown in Fig. 3. The length from the model center to the inlet is set to $30B$, and the length from the model center to the outlet is set to $60B$, which are in accordance with the recommendation by Tominaga *et al.* (2008). Aiming to compare the simulation results with wind tunnel measurements, the cross-section of the wind tunnel test section is used for the computational domain, i.e., the height of the computational domain is $25B$, and the width is $30B$, resulting in a reasonable BR of 0.8%, which is lower than the maximum of 3.0% suggested by the guidelines of Franke *et al.* (2007).

In the present simulations, a structured mesh is adopted for the entire computational domain. For the LES, a very fine mesh with prism layers around the building is required. According to the law of the wall, the distance of the first grids to the model surface (denoted by Δy) should be sufficiently small to ensure y^+ is less than 5, where $y^+ = \rho u_\tau \Delta y / \mu$. Thus, 50 grid layers are generated in the viscous boundary layer near the building surface, and the height of the first boundary layer is chosen to be $\delta / H = 1.1 \times 10^{-4}$ with a growth factor of 1.05, which satisfies the recommendation by Thordal *et al.* (2019). On the surfaces of the building model, the grid dimensions in the x , y and z directions are $\delta_x / H = \delta_y / H = 5.3 \times 10^{-3}$ and $\delta_z / H = 8.3 \times 10^{-3}$, respectively. In addition, the no-slip wall boundary conditions are used for the top and side boundaries, and the first grid wall distance to those boundaries is set as $\delta / H = 1.67 \times 10^{-3}$. For this mesh scheme, a bidirectional growth factor in the vertical and lateral directions is 1.05 and the grid stretching ratio in the wake region is restricted to less than 1.08. A view of the overall grid distribution can be observed in Fig. 4. Finally, the total grid numbers of the Case 1 simulation for the main computational domain are approximately 6.6 million (M1). For the purpose of the grid independence check, a mesh scheme (M2) of Case 1 with 4.9 million cells is also generated, and the first grid wall distance to the building surface is $\delta / H = 2.0 \times 10^{-4}$. In view of the very similar numerical results of the two mesh schemes (M1 and M2), the results based on the refined mesh scheme M1 are given in the following sections.

For the other five cases with higher BRs, as shown in Table 1, the grid topology is actually structured and the detailed parameters are nearly the same as in Case 1 (M1).

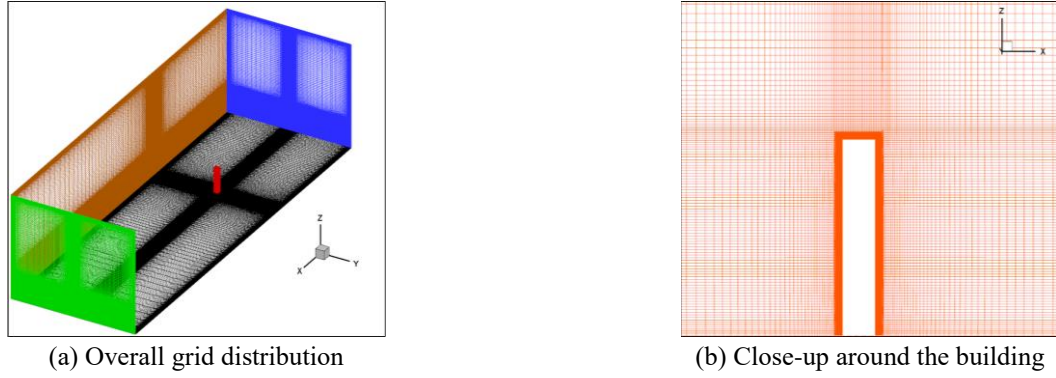


Fig. 4 Structured mesh scheme (M1) for the Case 1 numerical simulation

Table 2 Target wind field characteristics

Parameters	Definitions	Values
Mean velocity	$U_{avg}(z) = \frac{u_*}{\kappa} \ln\left(\frac{z+z_0}{z_0}\right)$	$u_* = 0.577 \text{ m/s}$ $z_0 = 2.25 \times 10^{-4} \text{ m}$
Turbulence intensities	$I_u(z) = a - b \ln(z+z_0) \quad (\text{Zheng et al. 2012})$ $I_v(z) = I_u(z) \frac{\sigma_v}{\sigma_u} \quad (\text{ESDU 85020, 2001})$ $I_w(z) = I_u(z) \frac{\sigma_w}{\sigma_u} \quad (\text{ESDU 85020, 2001})$	$a = 0.05665$ $b = 0.04316$
Turbulence integral scales	$L_u(z) = 100 \cdot \left(\frac{z}{30 \cdot \lambda_L}\right)^{0.5} / \lambda_L \quad (\text{AIJ, 2004})$ $L_v(z) = 0.5 \left(\frac{\sigma_v}{\sigma_u}\right)^3 L_u(z) \quad (\text{ESDU 85020, 2001})$ $L_w(z) = 0.5 \left(\frac{\sigma_w}{\sigma_u}\right)^3 L_u(z) \quad (\text{ESDU 85020, 2001})$	
von Karman turbulent spectra	$S_u(f) = \frac{4(I_u U_{avg})^2 (L_u / U_{avg})}{\left[1 + 70.8(fL_u / U_{avg})^2\right]^{5/6}}$ $S_v(f) = \frac{4(I_v U_{avg})^2 (L_v / U_{avg}) (1 + 188.4(2fL_v / U_{avg})^2)}{\left[1 + 70.8(2fL_v / U_{avg})^2\right]^{11/6}}$ $S_w(f) = \frac{4(I_w U_{avg})^2 (L_w / U_{avg}) (1 + 188.4(2fL_w / U_{avg})^2)}{\left[1 + 70.8(2fL_w / U_{avg})^2\right]^{11/6}}$	

In the streamwise direction, the grid spacing is identical for all six cases. In the regions near the building model, top boundary and side boundaries, the grid distributions are restricted to be fully consistent. All 6 cases have the same growth factors in the vertical and lateral directions.

3.2 Boundary conditions

The boundary conditions of the computational domain in the present work are also shown in Fig. 3. In order to

investigate the effects of the walls on the flow field and on the forces experienced by the building model, no-slip wall boundary conditions are applied to the upper and lateral boundaries, where the normal and tangential velocities are zeros. The inlet uses a velocity-inlet boundary, and the outlet uses an outflow boundary condition. Additionally, the no-slip wall boundary conditions are used on the ground and building surfaces.

An appropriate turbulent inflow boundary condition is very important for the accuracy of LES evaluation. For this

purpose, various researchers (Smirnov *et al.* 2001, Xie and Castro 2008, Huang *et al.* 2010; Patruno and Ricci 2017, Yu *et al.* 2018, Feng *et al.* 2019) have developed different inflow generation methods using the LES modeling approach. In the present study, the turbulent inflow is generated using the NSRFG technique, which satisfies the turbulence characteristics, including the divergence-free condition, coherency and correlation function, and turbulent spectra of the natural ABL flow. The details of the NSRFG technique are provided by Yu *et al.* (2018). Table 2 summarizes the physical turbulent statistical parameters of the target wind fields including mean velocity, turbulence intensities, turbulence integral scales, and von Karman turbulent spectra. The mean wind velocity, $U_{avg}(z)$, and turbulence intensity profiles, $I_u(z)$, are obtained by fitting the measured data from the wind tunnel (Zheng *et al.* 2012), and the values of fitted parameters u^* , z_0 , a and b are also shown in Table 2. According to ESDU 85020 (2001), σ_v/σ_u and σ_w/σ_u are defined as follows:

$$\frac{\sigma_v}{\sigma_u} = 1 - 0.22 \cos^4 \left(\frac{\pi z}{2h} \right) \quad (1)$$

$$\frac{\sigma_w}{\sigma_u} = 1 - 0.45 \cos^4 \left(\frac{\pi z}{2h} \right) \quad (2)$$

where h represents the height of the ABL. In the following sections, the variations in the pressure coefficients and aerodynamic forces on the building model and flow field characteristics with respect to the BR under the turbulent ABL flow are analysed in detail. Moreover, to investigate the influence of the characteristics of the incoming wind field on the blockage effects, other simulations are conducted in a uniform smooth inflow, and the inlet velocity is uniformly distributed without perturbations. The simulation cases under the turbulent inflow and uniform smooth inflow are represented by Case i_T and Case i_S respectively, wherein i is the case number and $i = 1 \sim 6$ (representing different BRs).

As mentioned above, this study includes 6 simulation cases in the turbulent inflow in order to investigate the impact of blockage on the assessment of wind effects on tall buildings, and higher BRs are obtained by changing the cross-section of the computational domain. For the sake of comparability, the consistency of the flow characteristics at the model location in different simulation cases needs to be ensured. Prior to the simulations of the building model in turbulent inflow, several simulations in the empty domain were performed to obtain the target mean wind velocity and turbulence intensity profiles, which are shown in Fig. 5. The mean wind velocity profiles $U_{avg}(z)$ and turbulence intensity profiles in the x direction $I_u(z)$ from different simulation cases were reproduced quite well with the measured data from the wind tunnel test. The normalized power spectral densities (PSDs) of the streamwise velocity components at the building height are given in Fig. 6. The results show that the spectra simulated in the present study are in good agreement with the von Karman spectrum over a wide frequency range, indicating that the turbulent inflow simulated in all present cases satisfies the turbulent spectra

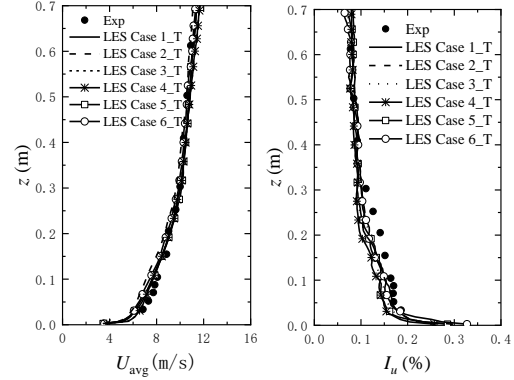


Fig. 5 Turbulent flow profiles from experimental data and generated by the NSRFG technique

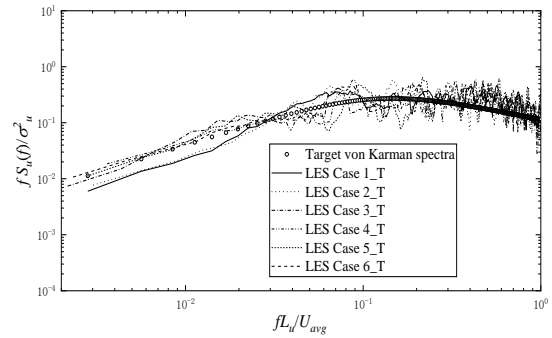


Fig. 6 Spectra of the velocity time histories obtained from LES in along-wind direction

of the ABL flow. According to these results, it can be concluded that the flow field characteristics (including the time-averaged wind velocity, turbulence intensity, and wind speed spectrum) at the model location in different simulation cases are maintained with good consistency. For the turbulent flow field, the wind velocity $U_H = 10.8$ m/s and the turbulence intensity $I_u = 8\%$ at the building height. For the uniform smooth inflow field, the velocity at the inlet is a constant value $U = 10.8$ m/s and without perturbations. Then, the Reynolds number of the simulations and experiments can be calculated as $Re = \rho U_H B / \mu = 7.39 \times 10^4$.

3.3 Numerical settings

The CFD code ANSYS Fluent 14.0 (Fluent 2011) was used to solve the governing equation. For all cases, the dynamic Smagorinsky-Lilly (Germano *et al.* 1991) model was used in this study, and the SIMPLEC algorithm was adopted for the pressure-velocity coupling. The second-order implicit scheme was used for the time discretization, and the bounded second-order implicit scheme was used for the momentum discretization. All the simulations were executed with a time step size of 0.0005 s with a sampling frequency of 1000 Hz. A total of 12 s of flow time is calculated for each case, and the last 8 s of the simulated result was extracted for data analysis, which corresponds to $145 t^*$ (t^* is the dimensionless time, which is calculated as $t^* = t U_H / H$). Based on the procedure proposed by Bruno *et al.* (2010), the convergence of the drag coefficient (C_{Fx}) and lift

coefficient (C_{Fy}) for the cases with different BRs are verified. The results indicate that the sampling time used in this study is sufficient to achieve satisfactory convergence of results, at least up to the second-order statistics.

3.4 Definitions of the aerodynamic coefficients

The pressure coefficients on the surface of the building model are calculated as follows:

$$C_{pi} = \frac{P_i - P_0}{0.5\rho U_H^2} \quad (3)$$

where, P_i is the dynamic pressure, P_0 is the reference pressure, ρ is the air density and U_H is the mean velocity at the building height H .

The definitions of the local wind force coefficient, i.e., the along-wind force coefficient $C_D(z)$ and across-wind force coefficient $C_L(z)$, are as follows:

$$C_D(z) = \frac{F_D(z)}{0.5\rho U_H^2 A(z)}, \quad C_L(z) = \frac{F_L(z)}{0.5\rho U_H^2 A(z)} \quad (4)$$

where $F_D(z)$ and $F_L(z)$ are the local forces at the height of z in the streamwise x and transverse y directions, respectively, and $A(z)$ is the windward area corresponding to the grid points at building height z .

The aerodynamic base force coefficients of the building model, including the windward force coefficient (C_{fx}), leeward force coefficient (C_{bx}), drag coefficient (C_{Fx}), lift coefficient (C_{Fy}), across-wind base moment coefficient (C_{Mx}), and along-wind base moment coefficient (C_{My}), are defined below:

$$C_{fx} = \frac{F_{x,windward}}{0.5\rho U_H^2 BH}, \quad C_{bx} = \frac{F_{x,leeward}}{0.5\rho U_H^2 BH} \quad (5)$$

$$C_{Fx} = \frac{F_x}{0.5\rho U_H^2 BH}, \quad C_{Fy} = \frac{F_y}{0.5\rho U_H^2 BH} \quad (6)$$

$$C_{Mx} = \frac{M_x}{0.5\rho U_H^2 BH^2}, \quad C_{My} = \frac{M_y}{0.5\rho U_H^2 BH^2} \quad (7)$$

where B is the width of the building; $F_{x,windward}$ and $F_{x,leeward}$ represent the wind force on the windward and leeward surfaces of the model, respectively; F_x and F_y are the aerodynamic forces in the x and y directions, respectively; and M_x and M_y are the overturning moments around the x and y axes, respectively.

The mean and root-mean-square (RMS) values of the pressure coefficients, the aerodynamic force and moment (ψ) are denoted as $C_{\psi,mean}$ and $C_{\psi,rms}$, respectively.

The blockage factor (BF) is employed here to describe the effects of the blockage on the mean pressure distributions and aerodynamic force coefficient,

$$BF = \frac{\text{The pressure and force coefficients of cases with larger BRs}}{\text{The pressure and force coefficients of Case 1}} \quad (8)$$

4. Results and discussion

4.1 Validation of the simulation results

To check the accuracy of the simulations, the pressure coefficients simulated in Case 1_T are compared with the measured results from the wind tunnel test (Zheng *et al.* 2012). Fig. 7 shows a comparison of the mean pressure coefficients ($C_{p,mean}$) and RMS pressure coefficients ($C_{p,rms}$) at a height of $2/3H$. It can be seen from Fig. 7(a) that good agreement between the simulation results of $C_{p,mean}$ in Case 1_T and the experimental results can be obtained, although the former slightly overestimates the negative $C_{p,mean}$ on the leeward face. For the $C_{p,rms}$ presented in Fig. 7(b), the simulation results match the experimental results satisfactorily in general, especially on the windward and leeward surfaces. However, the RMS pressure coefficients on the lateral surfaces are underestimated. The cause of this deviation between the LES results and the wind tunnel test results might be found in the inflow characteristics (Huang *et al.* 2007; Dagneu and Bitsuamlak 2014; Ricci *et al.* 2018). It should be noted that more necessary information on inflow properties, such as the vertical profiles of turbulence intensities in the y and z directions, $I_v(z)$ and $I_w(z)$, were not mentioned in the wind test (Zheng *et al.* 2012). Additionally, the modeling and simulation parameters (Bruno *et al.* 2014; Wijesooriya *et al.* 2019), such as the subgrid-scale turbulence model and discretization, may produce discrepancies.

The simulation results of the local mean and RMS along-wind force coefficient ($C_{D,mean}$ and $C_{D,rms}$) and across-wind force coefficient ($C_{L,mean}$ and $C_{L,rms}$) are shown in Fig. 8, wherein these values are compared with the experimental results. The values of $C_{D,mean}$ have a slightly larger magnitude for simulation Case 1_T as a result of the discrepancies of the mean pressure on the leeward surface (Fig. 8(a)). For $C_{D,rms}$, the simulation results match the experimental results quite well. The values of $C_{L,mean}$ are almost zeros along the height. Fig. 8(d) shows that the $C_{L,rms}$ values in Case 1_T are slightly smaller than the experimental results, which correspond to the smaller $C_{p,rms}$ on the lateral surfaces for Case 1_T.

On the whole, the pressure coefficients and aerodynamic forces predicted by LES are generally satisfactory, despite some discrepancies between the numerical results and the experimental data. Furthermore, the feasibility and effectiveness of the turbulent inflow generation method (i.e., NSRFG) and the setting of numerical parameters are verified. The other simulation cases with different BRs in this study are carried out on the basis of the same conditions as Case 1_T.

4.2 Blockage effects on the wind pressure distributions

This section presents detailed comparisons of the blockage effects on the wind pressure distributions on the building surfaces from the cases under the turbulent inflow.

Fig. 9 shows a comparison of the mean pressure coefficients $C_{p,mean}$ over the building perimeter at heights of

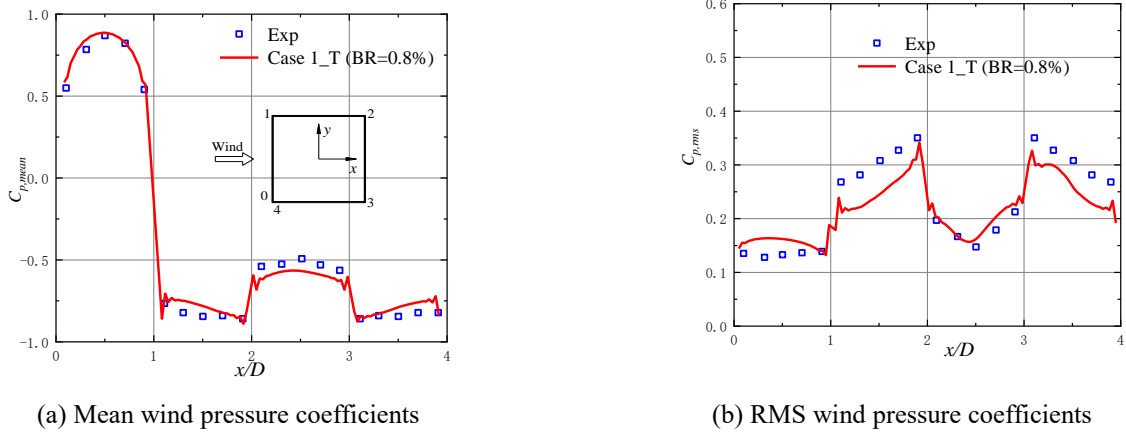


Fig. 7 Mean and RMS wind pressure coefficients at $2/3H$ in Case 1_T

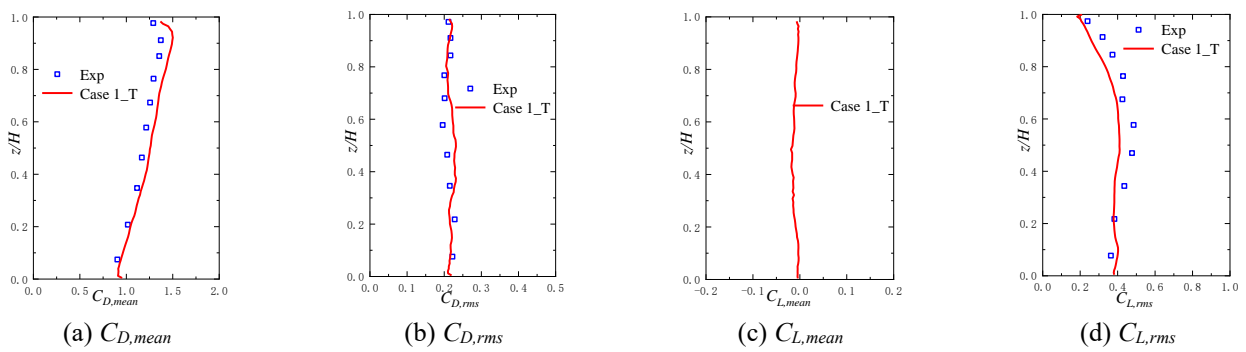


Fig. 8 Local aerodynamic forces along the building height from Case 1_T.

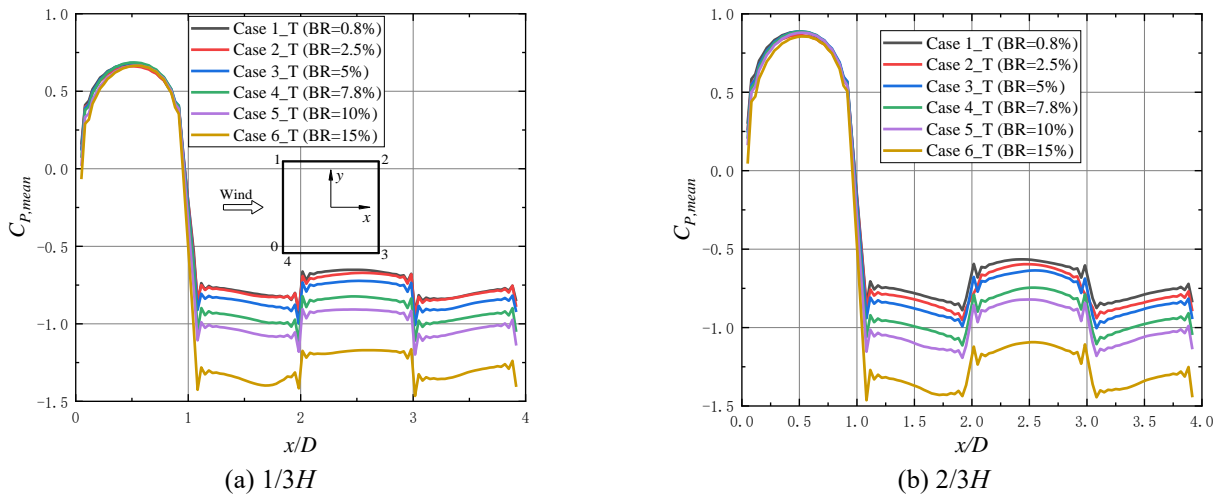


Fig. 9 Mean pressure coefficients at heights of $1/3H$ and $2/3H$ for the cases under turbulent inflow

$1/3H$ and $2/3H$ for the different BR cases under the turbulent inflow. On the windward surface, since the $C_{p,mean}$ is mainly influenced by the velocity profile of the approaching flow (Huang *et al.* 2007; Braun and Awruch 2009), $C_{p,mean}$ was found to be nearly consistent and not substantially affected by blockage for the simulation cases using similar gradient velocity profiles.

On the lateral and leeward surfaces, there is a small difference between the $C_{p,mean}$ of Case 1_T and Case 2_T, in which the BRs are 0.8% and 2.5%, respectively. However, with a further increase in the BR, the $C_{p,mean}$ becomes more

negative due to the reduction in the cross-sectional area of the computational domain. For Case 5_T (BR = 10%), the $C_{p,mean}$ on the lateral and leeward surfaces is approximately 32% and 40% higher than that in Case 1_T at $1/3H$ and $2/3H$, respectively. A more severe increase is noted for Case 6_T (BR = 15%), in which the $C_{p,mean}$ on the lateral and leeward surfaces is approximately 70% and 78% higher than that in Case 1_T at $1/3H$ and $2/3H$, respectively. It has been realized that the $C_{p,mean}$ values on the lateral and leeward surfaces are sensitive to both the inflow boundary conditions (Li and Melbourne 1995; Yan and Li 2015) and

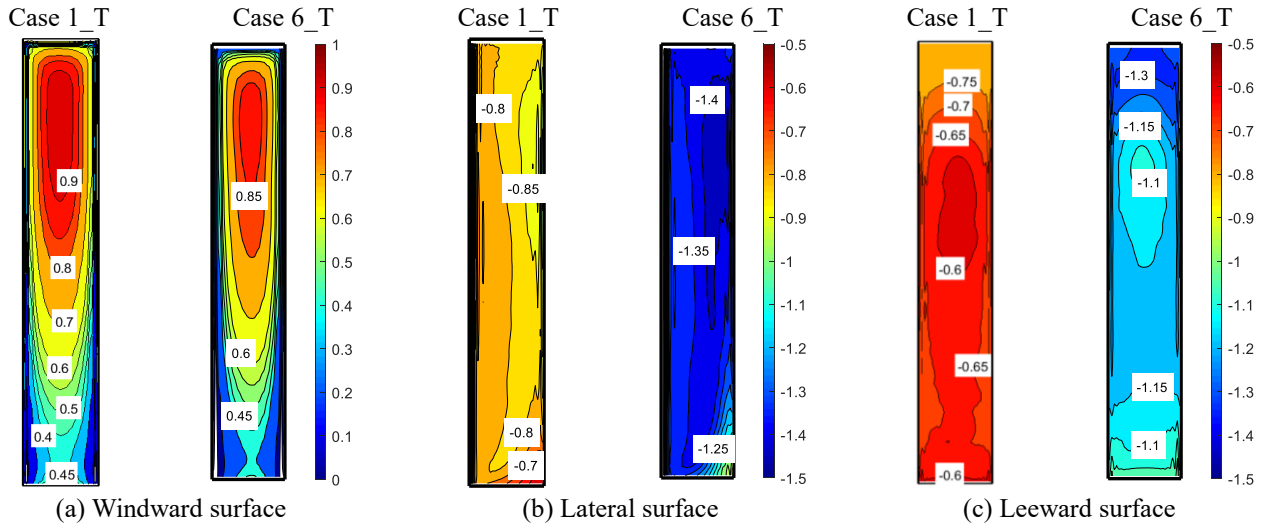


Fig. 10 Mean pressure coefficient contours for Case 1_T and Case 6_T

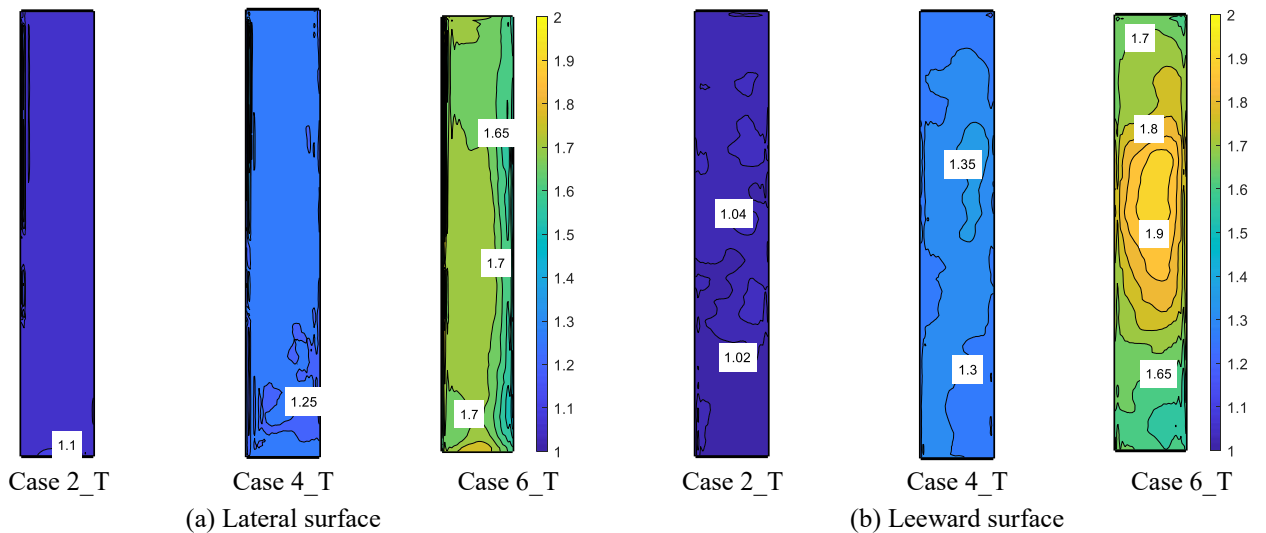


Fig. 11 BF contours of $C_{p, mean}$ on the lateral and leeward surfaces for Case 2_T ~ Case 6_T

the separation bubbles near the model surfaces (Thordal *et al.* 2019). Thus, the increase in the mean negative pressure can be explained as that the reduction in the cross-section enhances the body-induced turbulence and vortex shedding, which lead to a high suction on the lateral and leeward surfaces, and the larger the BR is, the higher the negative pressure occurs.

Fig. 10 shows the contours of the mean pressure coefficients on the building surfaces for Case 1_T and Case 6_T (not all six cases results are given herein due to limited space). On the windward surface (Fig. 10(a)), the $C_{p, mean}$ values are fairly similar although the cross-section of the computational domain has changed. On the lateral and leeward surfaces (Figs. 10(b) - (c)), which are affected by the flow separation and the wake flow, the $C_{p, mean}$ shows a strong negative pressure. The distribution patterns of the $C_{p, mean}$ are approximately consistent with the increase of BR, and a substantial increase is observed in the magnitude of the $C_{p, mean}$.

Moreover, Fig. 11 shows the BF (calculated by Eq. (8))

contour of the $C_{p, mean}$ on the lateral and leeward surfaces for Case 2_T, Case 4_T and Case 6_T. The following conclusions can be obtained from this figure. (1) for a smaller $BR \leq 2.5\%$, the BF on the lateral and leeward surfaces is less than 1.05, which means that the increase in the $C_{p, mean}$ is less than 5%, and the blockage effects is so weak that it can be ignored. (2) with the increase of BR, the distribution of BF becomes more inhomogeneous, indicating that the blockage effects of a three-dimensional building is more complicated. (3) the BF on the leeward surface is larger than that on the lateral surface; and the larger the BR is, the more significant the difference, meaning that the blockage has a stronger influence on the $C_{p, mean}$ on the leeward surface than that on the lateral surface.

The numerical RMS pressure coefficients $C_{p, rms}$ over the building perimeter at heights of $1/3H$ and $2/3H$ are presented in Fig. 12. On the windward surface, the $C_{p, rms}$ slightly increases with increasing BR because it is more sensitive to the turbulence intensity profile of the approaching flow (Huang *et al.* 2007, Thordal *et al.* 2019).

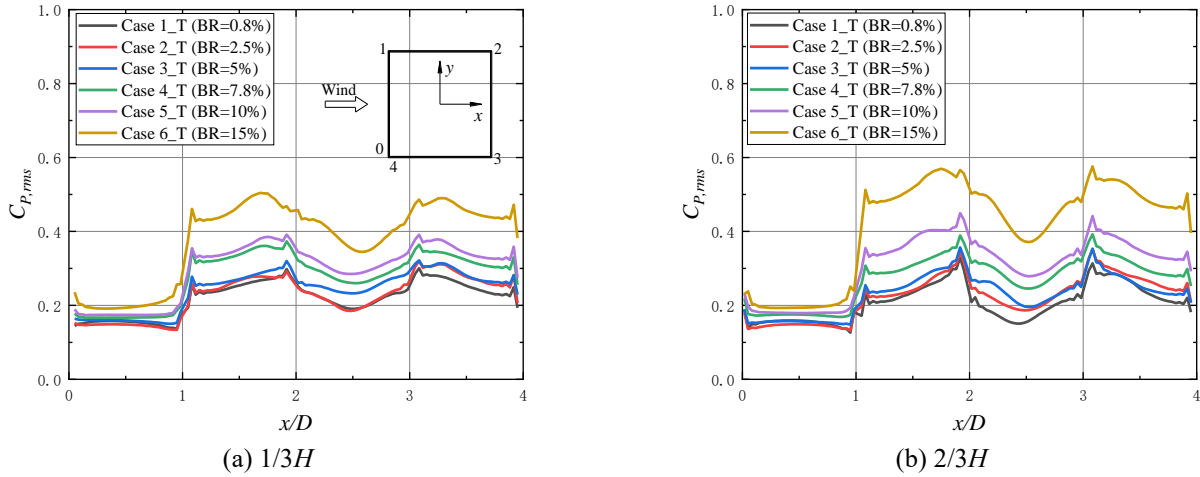


Fig. 12 RMS pressure coefficients at heights of $1/3H$ and $2/3H$ for the cases under turbulent inflow

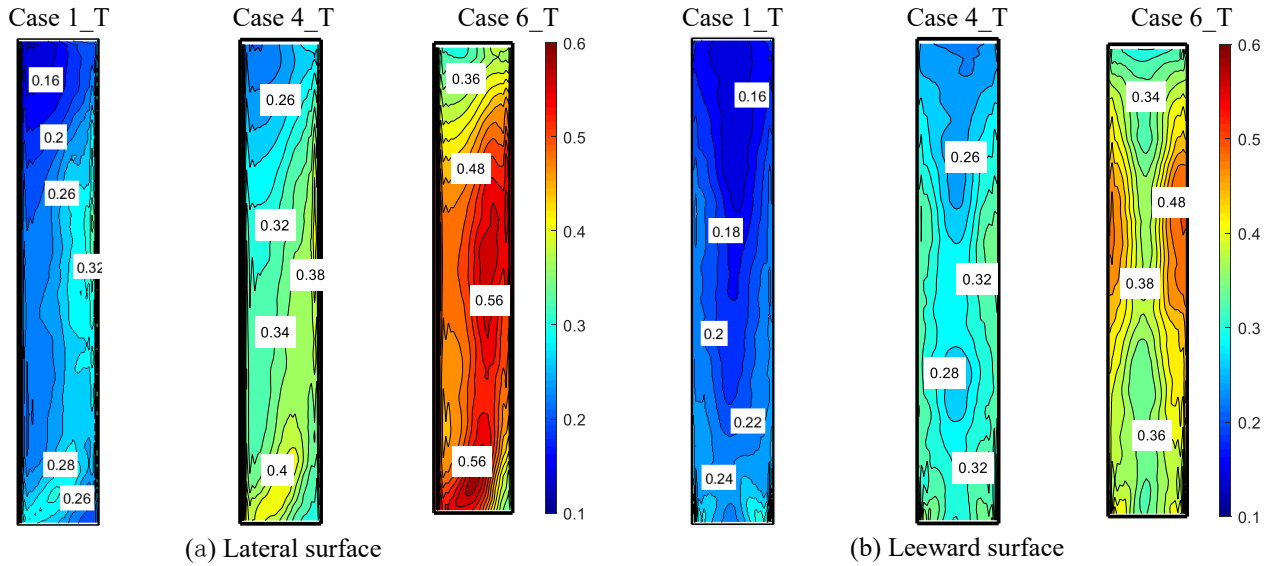


Fig. 13 RMS pressure coefficient contours for different simulation cases under turbulent inflow

To clarify the blockage effects on the fluctuating pressure distributions on the building surface, the contour plot of the $C_{p,rms}$ on the lateral and leeward surfaces for Case 1_T, Case 4_T and Case 6_T are shown in Fig. 13. On the lateral surface, the distribution patterns of $C_{p,rms}$ have hardly changed with increasing BR. However, the magnitude of $C_{p,rms}$ significantly increases as BR increases, and the maximum increase in $C_{p,rms}$ reaches up to 40% at BR = 7.8% and 120% at BR = 15% compared with Case 1_T. On the leeward surface, the $C_{p,rms}$ values are symmetrically distributed and the blockage does not change this distribution pattern. Similar to the lateral surface, the magnitude of $C_{p,rms}$ on the leeward surface significantly increases with increasing BR, and the maximum increase in $C_{p,rms}$ reaches up to 60% and 140% at BR = 7.8% and 15%, respectively.

In summary, the blockage effects on the $C_{p,rms}$ on the leeward surface are more serious than those on the lateral surface. In addition, it seems that the blockage effects on the $C_{p,rms}$ on the leeward and lateral surfaces are more serious than the corresponding effects on the $C_{p,mean}$.

4.3 Blockage effects on the aerodynamic force coefficients

In this section, the blockage effects on the aerodynamic forces of the building are discussed. The force and moment coefficients are calculated by Eqs. (5) - (7).

The time histories of the drag coefficient C_{Fx} and lift coefficient C_{Fy} obtained in the present simulations under the turbulent inflow are shown in Fig. 14. This figure shows that the fluctuation of the approaching flow causes high-frequency fluctuations of C_{Fx} in all cases (Fig. 14(a)). With the increase of BR, the fluctuation intensity of the drag time history is notably intensified, and the mean drag coefficient $C_{Fx,mean}$ increases significantly. Fig. 15(a) shows the variations in $C_{Fx,mean}$ with respect to BR, and the corresponding BFs are shown in Fig. 15(b). With the BR increasing from 0.8% to 5%, the $C_{Fx,mean}$ increases by 5% (from 1.28 to 1.35); when the BR reaches 15%, the $C_{Fx,mean}$ increases to 1.72 with an increase of 34% compared to that of Case 1_T. Additionally, the results of a two-dimensional square cylinder under high turbulence flow ($I = 11.2\%$)

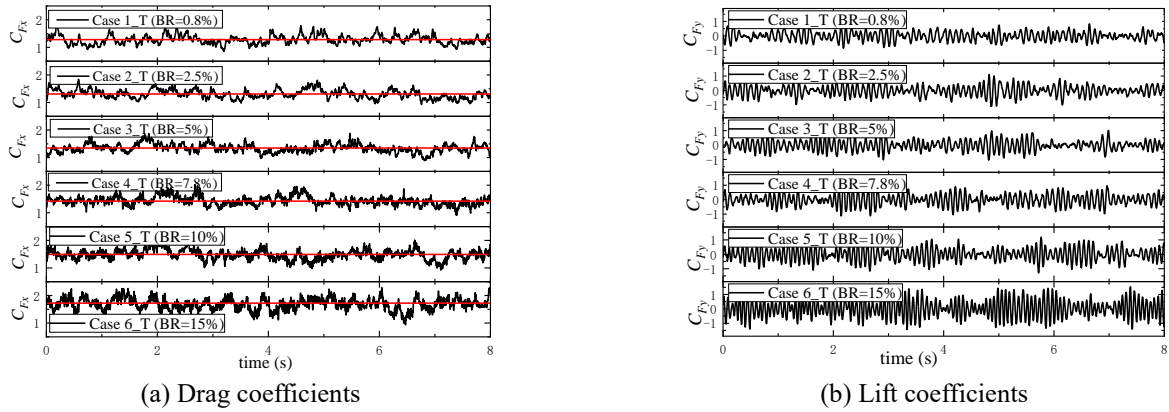


Fig. 14 Time histories of the drag and lift coefficients for different simulation cases under turbulent inflow

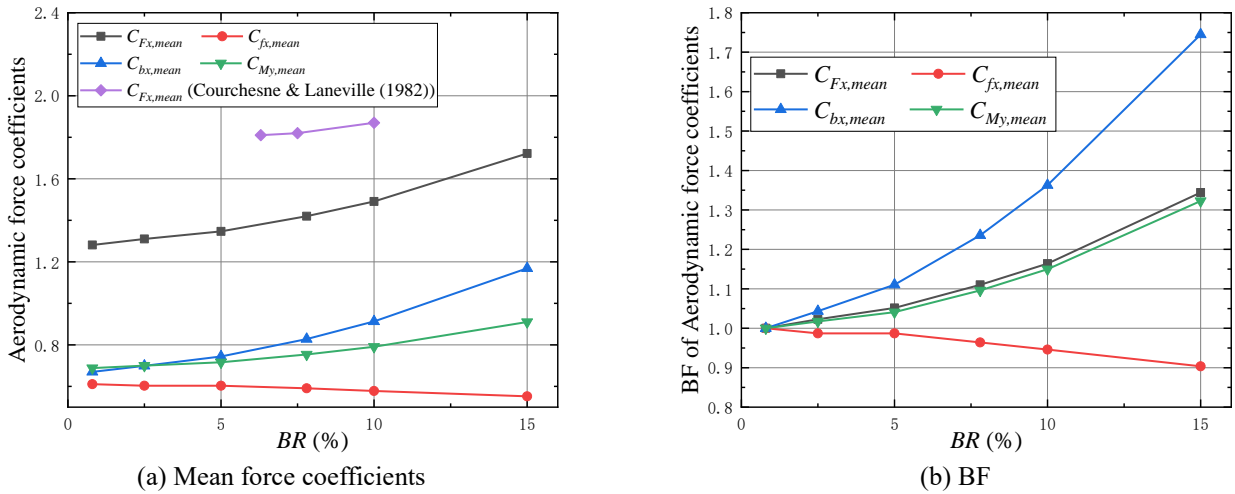


Fig. 15 Variations in the mean force coefficients and the corresponding BF with respect to BR

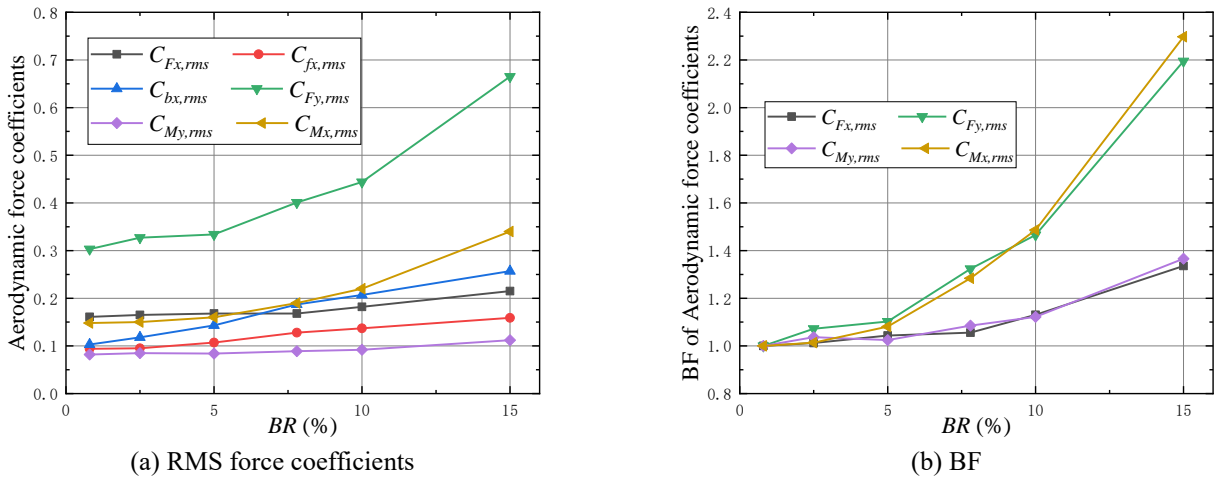


Fig. 16 Variations in the RMS force coefficients and the corresponding BF with respect to BR

performed in wind tunnel by Courchesne and Laneville (1982) are given in Fig. 15(a). In their study, the BR changes from 6.3% to 10%, and the $C_{Fx,mean}$ increases by 3%; and in the present simulations, the $C_{Fx,mean}$ increase by 10% with the BR increasing from 5% to 10%. As mentioned in Section 4.2, the blockage has a slight effect on the mean pressure on the windward surface. Therefore, the mean windward force coefficient $C_{fx,mean}$ and mean leeward

force coefficient $C_{bx,mean}$ (the absolute value) are considered separately as shown in Fig. 15. The results reveal that as the BR increases from 0.8% to 15%, the $C_{bx,mean}$ increases from 0.67 to 1.16, while the $C_{fx,mean}$ exhibits a slight decrease. In addition, the variations in the RMS drag coefficient $C_{Fx,rms}$, RMS windward force coefficient $C_{fx,rms}$ and RMS leeward force coefficient $C_{bx,rms}$ with respect to BR are shown in Fig.

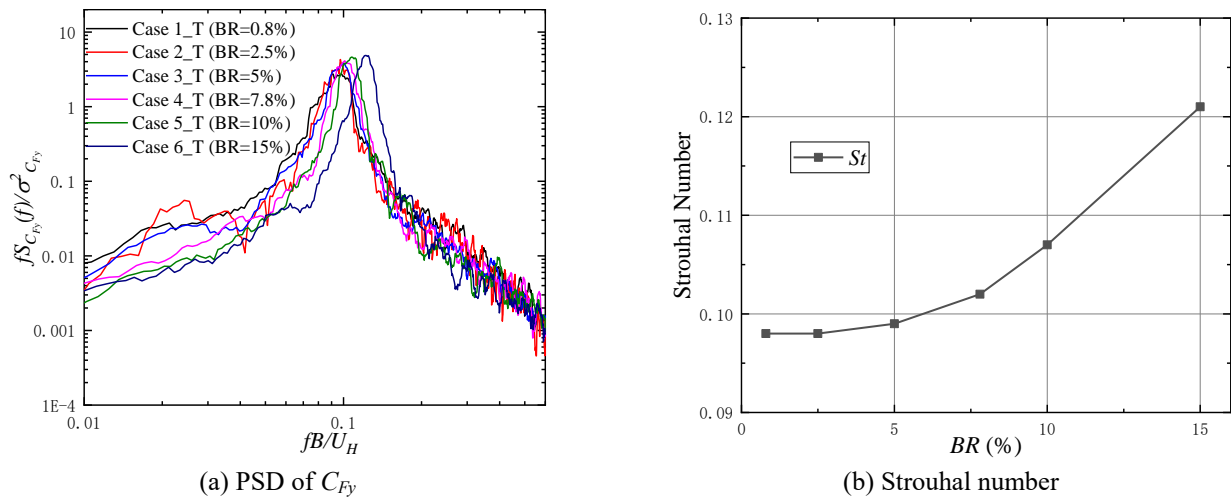


Fig. 17 PSD of the lift coefficients and corresponding St for the cases under turbulent inflow

16. All these fluctuation force coefficients increase monotonically with increasing BR, and the increases in $C_{bx,rms}$ is more obvious. With the BR increasing from 0.8% to 5%, the increase ratios of $C_{Fx,rms}$ is 4%, and the increase ratio is 33.5% when the BR reaches 15%. The results indicate that the increase in the mean drag coefficient is entirely due to the increase in the mean suction coefficient on the leeward surface, while the increase in the RMS drag coefficient is influenced by both windward and leeward forces, of which the latter is more prominent.

Fig. 14(b) shows that the time histories of the lift coefficient C_{Fy} for different blockage cases under the turbulent inflow vary regularly and periodically with respect to time, which is associated with the existence of organized vortex shedding. With the increase of BR, the fluctuation frequency increases, which reveals that the frequency of vortex shedding increases; the amplitude of fluctuation C_{Fy} increases, which means that the RMS lift coefficient $C_{Fy,rms}$ becomes larger, as shown in Fig. 16(a). With the BR increasing from 0.8% to 15%, the $C_{Fy,rms}$ increases from 0.3 to 0.66 with an increase ratio of 120%. The normalized PSDs of C_{Fy} for the six cases are shown in Fig. 17(a). Sharp peaks can be observed at the vortex shedding frequency in all cases, and both the vortex shedding frequency and peak value increase with the increasing BR, indicating that the intensity of the vortex shedding has been markedly strengthened by the blockage. The Strouhal number St calculated from the spectral peaks is plotted against the BR in Fig. 17(b), where $St = fB/U_H$ and f is the shedding frequency. With the BR increasing from 0.8% to 15%, St increases from 0.098 to 0.12 with an increase ratio of 23%. It is evident from the results that $C_{Fy,rms}$ is more significantly affected by the blockage than $C_{Fx,rms}$.

Moreover, the mean and RMS base moment coefficients and the corresponding BF are also shown in Figs. 15 and 16. The $C_{My,mean}$ increases monotonically with increasing BR, and the BFs of the $C_{My,mean}$ and $C_{Fx,mean}$ are very close to each other at different BRs (Fig. 15(b)), it means that the blockage has almost the same effects on them. Similar observations are made for the comparisons between $C_{Fx,rms}$

and RMS along-wind base moment coefficient $C_{My,rms}$ and between $C_{Fy,rms}$ and RMS across-wind base moment coefficient $C_{Mx,rms}$, as shown in Fig. 16.

For the square building model with sharp edges, the $C_{p,rms}$ on the lateral and leeward surfaces are influenced by both the flow characteristics of the approaching flow and the fluctuation due to flow separation (Dagnev and Bitsuamlak 2013). Fig. 12 shows that the $C_{p,rms}$ on the lateral and leeward surfaces increase significantly with increasing BR, especially for Case 6_T (BR = 15%). Thordal *et al.* (2019) noted that the lateral and leeward surfaces of a sharp-edged building will be inside the separation bubbles and affected by body-induced turbulence and vortex shedding. Since the inflow conditions in the present study are approximately the same as shown in Fig. 5, it is more reasonable to conclude that the confinement of the boundary walls forces the flow to accelerate when it passes through the region near the model, and the interaction between the model and the fluid will be strengthened leading to the increases in the RMS pressure on the lateral and leeward surfaces. This phenomenon becomes more serious when the BR increases.

4.4 Blockage effects on the time-averaged flow fields

In contrast to wind tunnel tests, CFD provides a detailed visualization of flow fields, which is a prominent advantage. The mean flow fields in Case 1_T, Case 3_T, Case 5_T and Case 6_T are compared to further investigate the influences of blockage.

Fig. 18 shows the mean pressure coefficients contour with time-averaged streamlines on the vertical ($X-Z$) plane at $y=0$, and the time-averaged streamlines on the horizontal ($X-Y$) plane at $z=2/3H$ are shown in Fig. 19. The turbulent inflow approaching the building leads to a high positive pressure field in front of the building, and a horseshoe vortex forms and wraps around the building model near the ground (Martinuzzi and Tropea 1993). The comparison of the simulation results from the four cases shows that the differences in the flow patterns upstream from the building are negligible because they are mainly

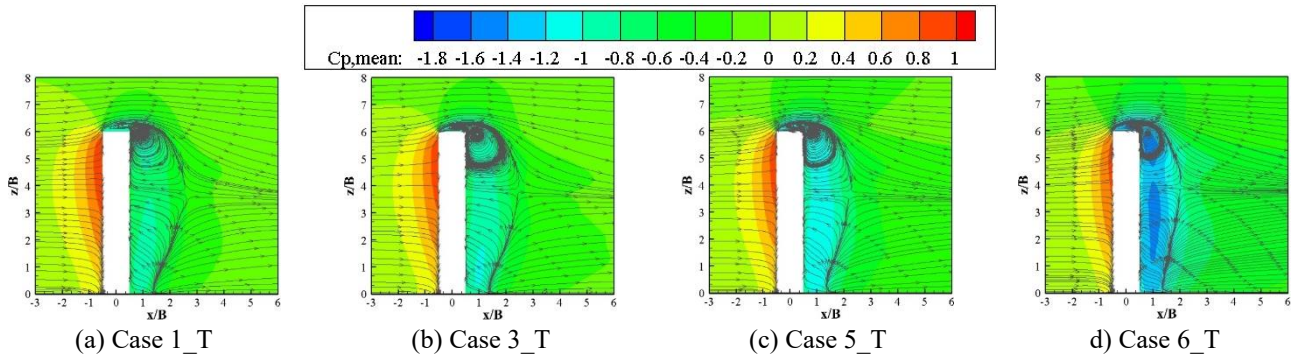


Fig. 18 Mean pressure coefficients contour with the time-averaged streamlines on the X - Z plane at $y = 0$

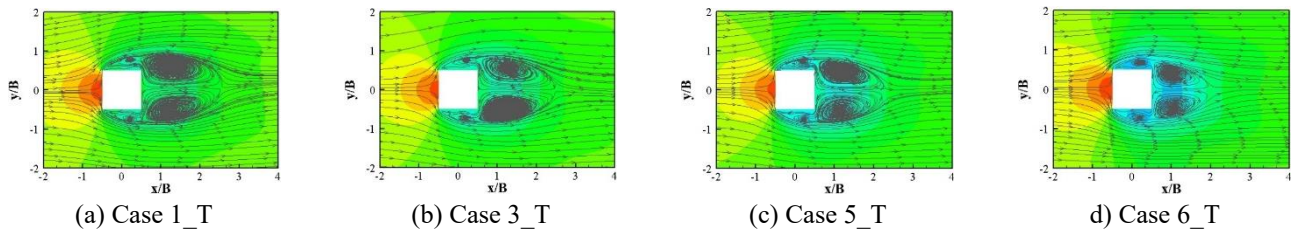


Fig. 19 Mean pressure coefficients contour with time-averaged streamlines the on X - Y plane at $z = 2/3H$

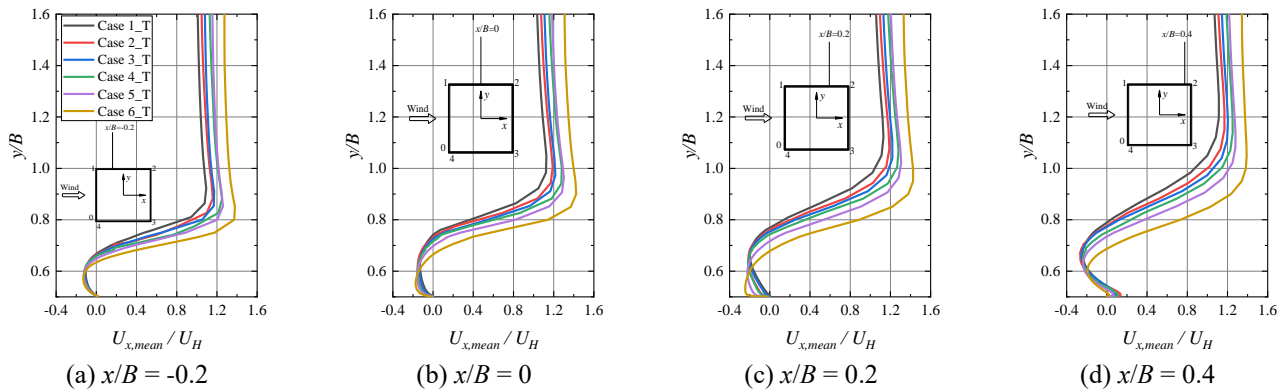


Fig. 20 Profiles of velocity along the transverse direction in the separation region at $2/3H$

influenced by the physical properties of the incident flow (Huang *et al.* 2007).

Fig. 18 shows that a large recirculation region exists just downstream of the building top which is principally generated from the separated shear layer and draws the flow back towards the building. A pair of counter-rotating vortices is identified downstream of the building as shown in Fig. 19. Huang *et al.* (2007) noticed that the contraction of the recirculation region behind the building model is always in accordance with a stronger base suction and a higher drag force. The flow patterns predicted by the current numerical study show that the differences between the different cases are mainly embodied in the sizes of the recirculation region and the location of the vortex in the wake regions behind the building. For Case 1_T, the vortex is at the most downstream location and the recirculation region behind the building has the largest size in transverse and streamwise directions, which is in accordance with its least negative pressure on the leeward surface and minimum $C_{Fx,mean}$ of the building. With the increase of BR, the vortex moves closer to the building and the sizes of the

recirculation region decrease obviously both in the transverse and streamwise directions. The smaller recirculation region size is in accordance with the larger $C_{Fx,mean}$ and higher negative pressure on the leeward surface of the building.

Moreover, the approaching flow is fully separated at the leading edge and develops a separation region near the roof and lateral surfaces of the model. Fig. 20 shows the profiles of the time-averaged streamwise velocity at several locations along the transverse direction within the separation region at $2/3H$. The results show that with the increase of BR, the separation boundary layer is compressed and the thickness decreases gradually. Meanwhile, the time-averaged streamwise velocity at the outer boundary of the separated shear layer increases up to the side boundaries. In addition, as the flow passed over the building from the top and side regions, high negative pressure fields are formed in these regions. Visually, the increase in the BR leads to higher negative pressure at these locations, especially behind the leeward surface of the building.

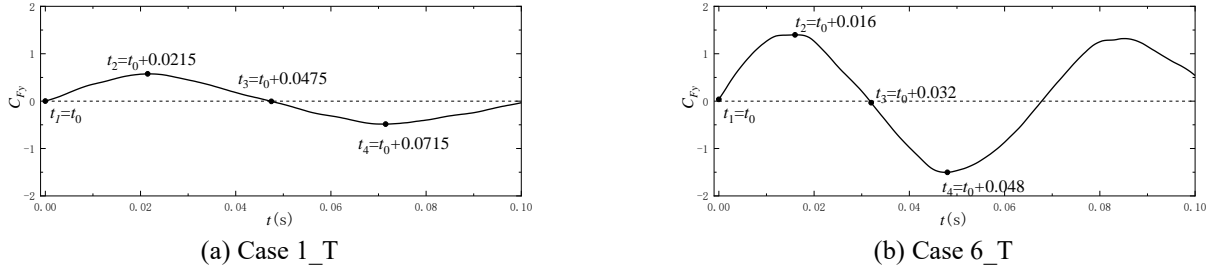


Fig. 21 Selected instants in the time histories of the lift coefficients for Case 1_T and Case 6_T

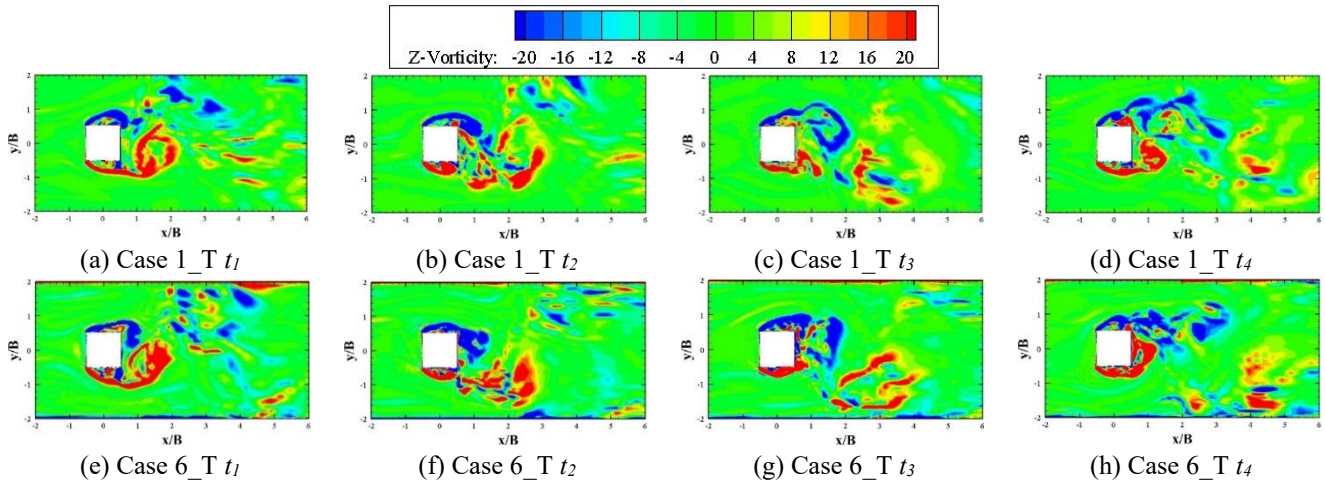


Fig. 22 Time evolutions of the instantaneous z-vorticity contours on the horizontal plane at the height of $2/3H$ for Case 1_T and Case 6_T

4.5 Blockage effects on the instantaneous flow fields

Based on the instantaneous simulation results of Case 1_T and Case 6_T, the flow fields during one period of the lift coefficient are selected for comparison to investigate the blockage effects on the transient flow field. Four instants of each case, i.e., $t_1 \sim t_4$, are shown in Fig. 21. The time evolutions of instantaneous z-vorticity contours (normalized with H and U_H) on the horizontal ($X - Y$) plane at $2/3H$ for Case 1_T and Case 6_T are shown in Fig. 22. The following conclusions are drawn from a comparison of the results from Case 1_T and Case 6_T in which the BR is 0.8% and 15%, respectively. It is observed that: (1) Fig. 21 shows that the period of the vortex shedding for Case 6_T is much shorter than that for Case 1_T, that is, the Strouhal number increases obviously with the increase of BR (Fig. 17(b)). The main reason is that the larger BR leads to the more significant curved shear layer and the faster rolling up speed, thus, speeding up the formation and shedding of the vortex. (2) in the separation region near the side walls of the model, the increase of BR limits the transport space of the vortices and forces the shear layer to move closer to the surface of the model (Fig. 20). The increase in the vortex intensity enhances the interaction between the separation region and the model surface and leads to larger pressure fluctuations on the surfaces of the building. (3) the wake region behind the model is controlled by the vortices formed from the shear layers at the upper and lower sides

alternately. Due to the increase in the vortex shedding frequency and vortex intensity, the interaction between the wake region and the model surface also increases. Therefore, the fluctuating pressure on the model back surface increases obviously.

To provide more insight into the flow topology, turbulent structures in a three-dimensional instantaneous flow around the building are visualized in Fig. 23 by means of iso-surfaces of the second invariant of the velocity gradient tensor. This is the so-called Q -criterion, which can be written for an incompressible flow as follows (Hunt 1988):

$$Q = (\Omega_{ij}\Omega_{ij} - S_{ij}S_{ij})/2 \quad (6)$$

where S_{ij} is the strain rate tensor and Ω_{ij} is the rotation rate tensor.

Fig. 23 shows the Q iso-surfaces of Case 1_T and Case 6_T. The approaching flow separates at the front edge of the roof and side surfaces, and leads to the development of the separation region. The flow structures in the wake region of the building exhibit evident three-dimensional characteristics. For both cases, the flow features, such as vortex shedding phenomenon, base horse shoe vortex, separation vortices at sharp edges and abundant turbulent structures of different scales in the wake, can be observed. Moreover, the effects of wall confinement on the three-dimensional turbulent structures is obvious and the increase of BR leads to the formation of more complicated turbulent structures. For Case 1_T, the scale of the turbulent

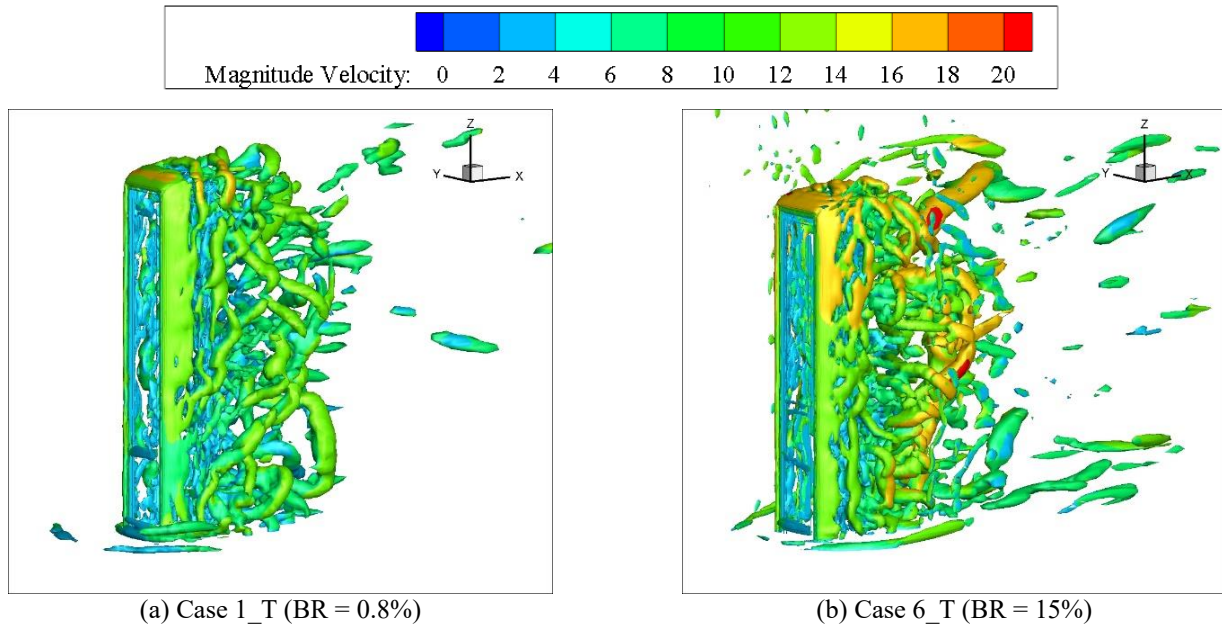


Fig. 23 Three-dimensional views of the flow topology: iso-contours of the instantaneous turbulent structures ($Q = 4 \times 10^4 \text{ s}^{-2}$) colored with the instantaneous velocity

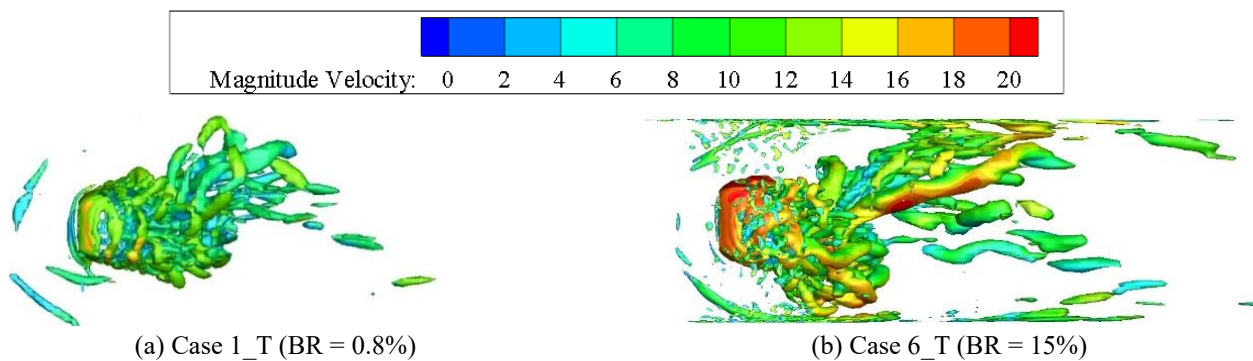


Fig. 24 Top views of the flow topology: iso-contours of the instantaneous turbulent structures ($Q = 4 \times 10^4 \text{ s}^{-2}$) colored with the instantaneous velocity

structures downstream the model is small and in a more scattered form, i.e., the integrity of the structures is weak; in contrast, for Case 6_T, the scale of the turbulent structures become larger and the integrity gets higher. These highly integrated coherent structures eventually increase the correlation among the wind loads at different heights, thereby impose the larger overall fluctuating wind forces (Fig. 16).

For the convenience of comparison, top views of the three-dimensional turbulent structures are shown in Fig. 24. The comparison of the results from Case 1_T and Case 6_T shows that as the BR increases from 0.8% to 15%, the complexity of the turbulent structures in the wake region increases obviously and the wake extends further downstream. In addition, abundant secondary vortices with a scale smaller than those shed from the building can be observed near the side and roof boundaries of the computational domain where the no-slip wall boundary conditions are used. In the case with higher blockage ratio, the vortices shed from the building move downstream in a

confined manner due to the severely restricted wall boundaries, and the interaction with the small-scale vortices near the no-slip wall boundaries of the computational domain becomes more significant.

The distributions of the mean wall shear stress on the side boundary of the computational domain at the building height of $2/3H$ from Case 5_T and Case 6_T are presented in Fig. 25, wherein the mean wall shear stress is normalized with U_H^2 ; thus, the effects of the building on the mean shear stress can be addressed. For both cases, the maximum values occur at $x/B = 0$, where the flow is accelerated due to the reduction in the cross-sectional area. In addition, the minimum values occur at $x/B = 2.3$ and $x/B = 1.5$ for Case 5_T and Case 6_T, respectively. The minimum shear stress occurs at the location where flow separation takes place on the side boundary of the computational domain (Schlichting and Gersten 2016), generating a smaller vortex that counter rotates against the vortices shed from the building (Kim *et al.* 2004) as shown in Figs. 23(b) and 24(b).

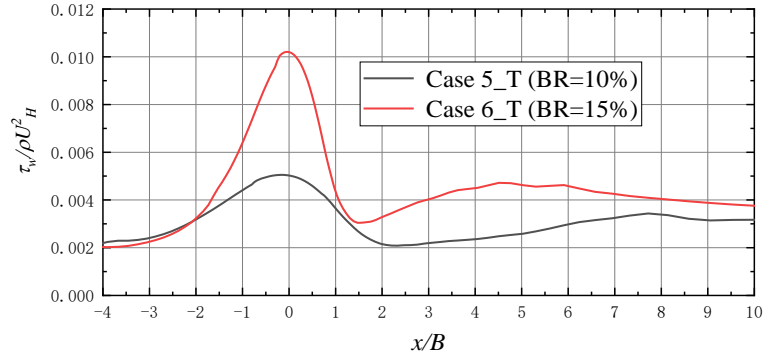


Fig. 25 Mean shear stress distribution along the side boundary at $2/3H$ for Case 5_T and Case 6_T

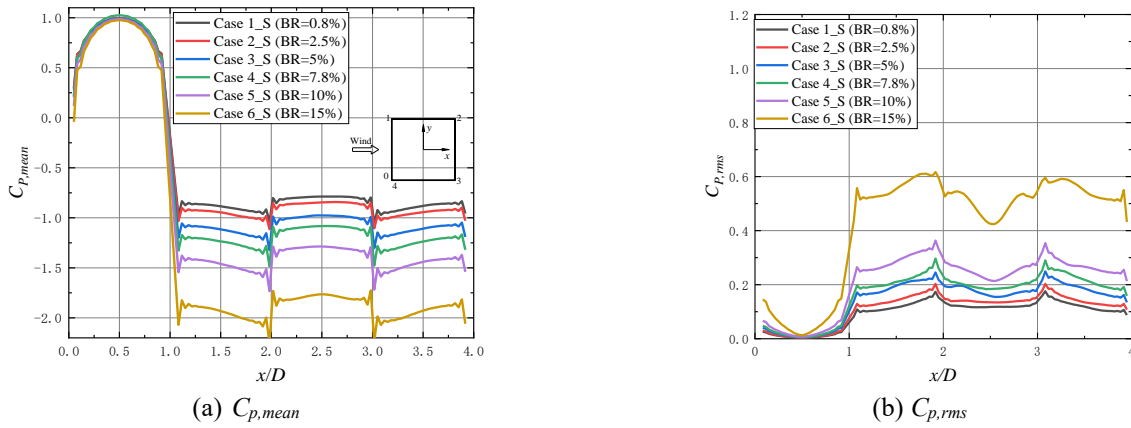


Fig. 26 Mean and RMS pressure coefficients at $2/3H$ of the model under uniform smooth inflow

4.6 Influence of the inflow properties on the blockage effects

The blockage effects on the aerodynamic forces and flow patterns around the tall building under the turbulent inflow are described above. In this section, the influence of inflow characteristics on the blockage effects is investigated by analysing the results from the cases under the uniform smooth inflow.

Fig. 26 shows the comparison of the mean pressure coefficients $C_{p,mean}$ and RMS pressure coefficients $C_{p,rms}$ over the building perimeter at a height of $2/3H$ for the different BR cases under the uniform smooth inflow. On the windward surface, a negligible discrepancy in the $C_{p,mean}$ exists among the cases with the same uniform smooth inflow but different BRs. In contrast, the $C_{p,mean}$ on the lateral and leeward surfaces is significantly affected by the blockage, and obviously decreases with the increase of BR. These findings are consistent with the results from the cases under the turbulent inflow, as mentioned in Section 4.3. However, a quantitative comparison of the results shows that the $C_{p,mean}$ is more significantly affected by the blockage for the cases under the uniform smooth inflow. For the lateral and leeward surfaces of $2/3H$ at BR = 5%, the $C_{p,mean}$ in Case 3_S is 25% larger on average than that in Case 1_S which is more significant than that between Case 3_T and Case 1_T. When the BR reaches 15%, the $C_{p,mean}$ in Case 6_S is 120% larger on average than that in Case 1_S, while the increase ratio is 78% between Case 6_T and Case

1_T. Moreover, a comparison of the BF contours of the $C_{p,mean}$ on the lateral and leeward surfaces clearly shows that the BF under the uniform smooth inflow is significantly larger than that under the turbulent inflow. Under the smooth inflow without perturbations, the $C_{p,rms}$ on the windward surface is smaller than that of the cases under the turbulent inflow. With the increase of BR, the $C_{p,rms}$ on the lateral and leeward surfaces increase obviously and the increase ratio is significantly larger than that under the turbulent inflow.

Fig. 27 plots the mean drag coefficient $C_{Fx,mean}$, mean windward force coefficient $C_{fx,mean}$ and mean leeward force coefficient $C_{bx,mean}$, and the corresponding BFs against BR for the cases under the smooth inflow. It can be observed that the variations of all these statistics are generally consistent with the results under the turbulent inflow mentioned above. However, the blockage effects on these statistics under the smooth inflow are more significant than those under the turbulent inflow. For instance, the increase ratios of $C_{Fx,mean}$ are 31% and 60% for Case 5_S and Case 6_S compared that with Case 1_S, respectively, however, $C_{Fx,mean}$ increases by 16% and 34% for Case 5_T and Case 6_T compared with Case 1_T, respectively. Additionally, as shown in Fig. 28 that the variations in the RMS aerodynamic forces and Strouhal number with respect to BR under the uniform smooth inflow are more serious than those under the turbulent inflow. These findings confirm that the blockage effects on the pressure coefficients and aerodynamic forces under the smooth inflow are much

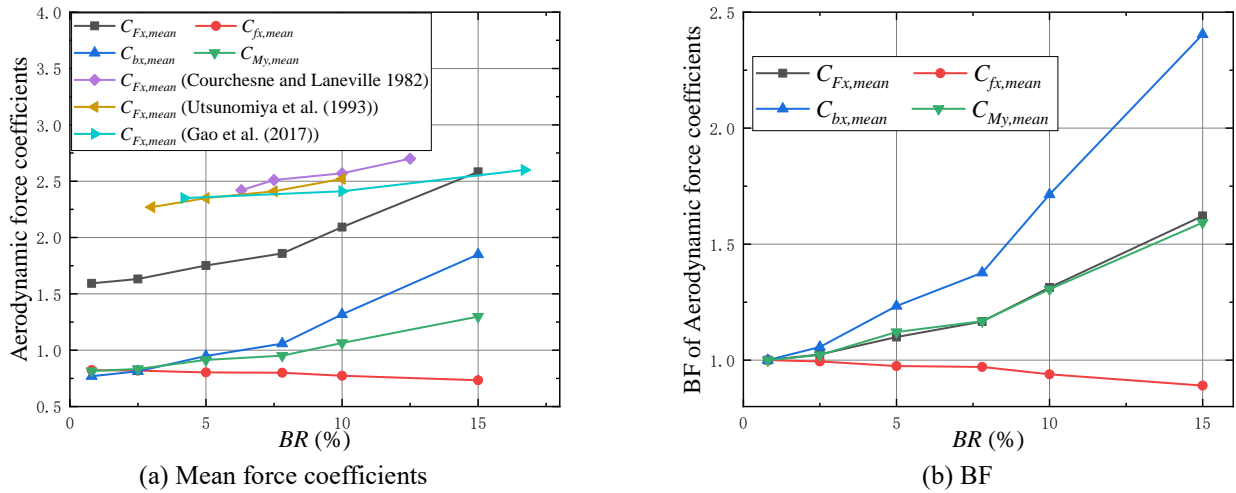


Fig. 27 Variations in the mean force coefficients and the corresponding BF with respect to BRs for the cases under uniform smooth inflow

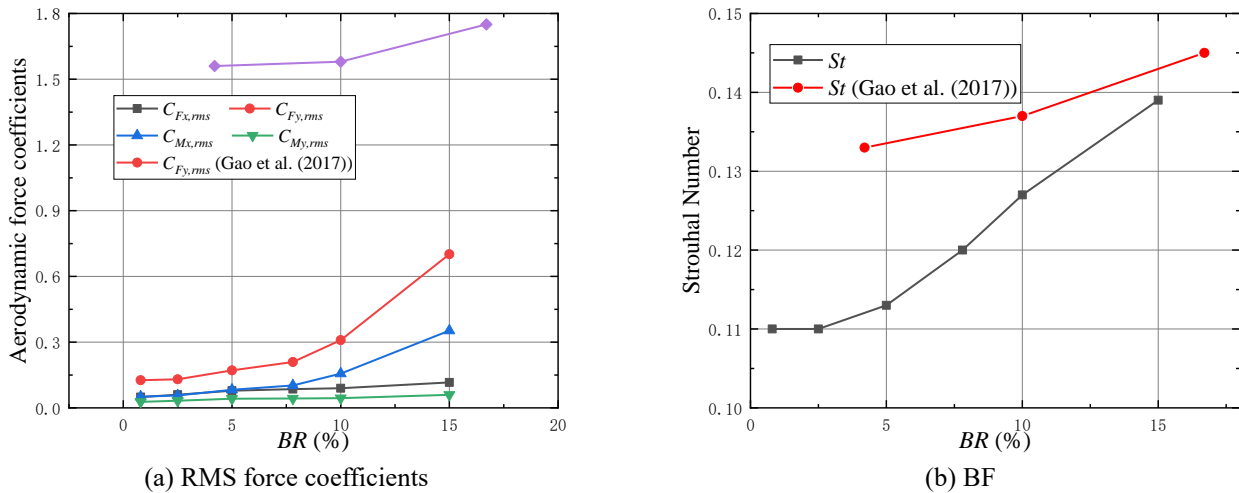


Fig. 28 Variations in the RMS force coefficients and the Strouhal number with respect to BRs for the cases under uniform smooth inflow

greater than those under the turbulent inflow. Moreover, the comparisons of the results for a two-dimensional square cylinder under the smooth inflow performed by wind tunnel (Courchesne and Laneville 1982, Utsunomiya *et al.* 1993) and LES (Gao *et al.* 2017) are also depicted in Figs. 27 and 28. It can be clearly found that the difference between the blockage effects of the two-dimensional bluff bodies and three-dimensional high-rise buildings is noticeable. The latter is more affected by the blockage.

The mean flow fields for Case 1_S and Case 6_S are selected to investigate the blockage effects on the flow field under the uniform smooth inflow. The time-averaged streamlines with the contour of mean pressure coefficients on the horizontal (X - Y) plane at $2/3H$ for Case 1_S and Case 6_S are given in Fig. 29. It can be observed that with the increase of BR, the size of the recirculation region behind the building decreases obviously and the vortex centre moves upstream. Moreover, the lateral shear layers move closer to the side faces of the building. These effects are similar to those under the turbulent inflow and consistent with the significant increase in the negative

$C_{p,mean}$ on the lateral and leeward surfaces (Fig. 26) and the increase in the mean wind forces (Fig. 27). In order to compare the average wake flow characteristics under the smooth inflow and turbulent inflow more visually, Fig. 30 presents the contours of $U_{x,mean} = 0$ on the X - Y plane at $1/3H$ and $2/3H$ from the cases under the turbulent inflow and those at $2/3H$ from the cases under the smooth inflow, which can be used to determine the position of the flow separation and the recirculation region in the wake region. It should be noted that this contour cuts each of the vertex loops in half; thus, the enclosed region is smaller than the wake presented in Figs. 19 and 29. It clearly shows that the increase of BR leads to a decrease in the size of the recirculation region in the wake, which is more serious for the cases in the smooth inflow. The recirculation length, i.e., the distance from the rear surface of the model to the node (marked as "I" in Fig. 29), reduces from $2.8B$ at $BR = 0.8\%$ to $1.9B$ at $BR = 15\%$ on the X - Y plane at $2/3H$ under the smooth inflow, while the corresponding length reduces from $2.0B$ to $1.6B$ at $1/3H$ and from $2.5B$ to $2.0B$ at $2/3H$ under the turbulent inflow. In addition, with the increase of BR,

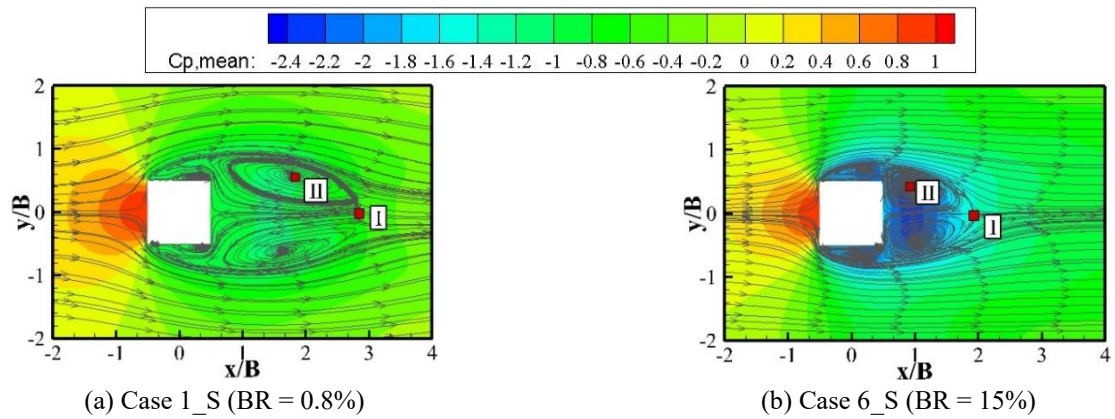


Fig. 29 Time-averaged streamlines with the contour of mean pressure coefficients on X - Y plane at $z = 2/3H$

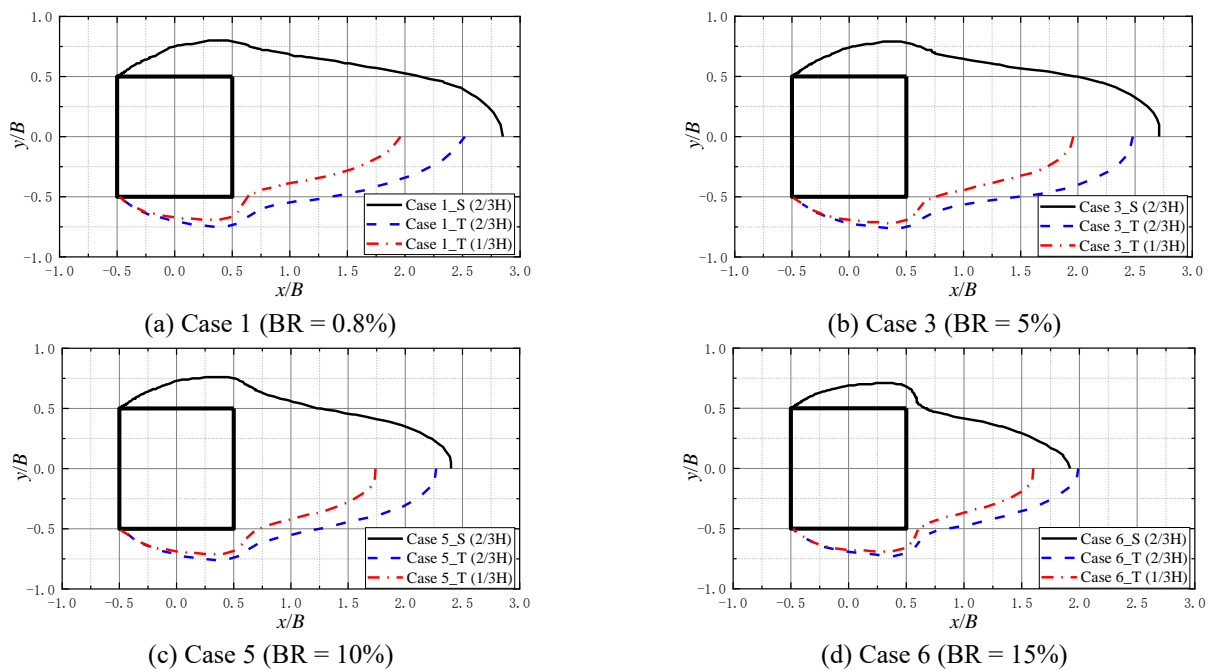


Fig. 30 Contour of $U_{x,mean} = 0$ in the X - Y plane

the contours of $U_{x,mean} = 0$ on the lateral side of the model move closer to the surface in smooth inflow as shown in Fig. 30. As the smooth inflow can delay the development of vortex shedding (Zhang *et al.* 2015), the center point (marked as “II” in Fig. 29) of the counter-rotating vortices behind the model are located at $x/B = 1.8$ at $2/3H$ for Case 1_S, while the corresponding location is $x/B = 1.3$ at $2/3H$ for Case 1_T. On the other hand, with the increase of BR, the centre of the vortices under the turbulent inflow and under the smooth inflow moves upstream to $x/B=1.0$ and $x/B = 0.9$ for Case 6_T and Case 6_S at $2/3H$, respectively, indicating that the blockage effects on the counter-rotating vortices under the smooth inflow are more significant.

A possible reason why the effects of blockage are more significant for smooth incoming flow than for the turbulent inflow can be explained as follows: Under the uniform smooth inflow, the periodicity and integrity of vortex shedding on both sides of the model are more evident (the frequency of vortex shedding becomes larger), and the separated shear flow and wake flow are generally wider

than those under turbulent inflow (Fig. 30). These flow features are more susceptible to the blockage, leading to much stronger blockage effects on the pressure and aerodynamic forces of the building in smooth inflow than those under the turbulent inflow.

5. Conclusions

In the present study, the blockage effects on the aerodynamic forces and flow patterns of a square tall building were investigated via LES under the uniform smooth inflow and turbulent ABL flow, the latter was generated by means of the NSRFG method. First, the inflow turbulence generation technique (i.e., NSRFG) and numerical simulation method were verified through the comparison with the wind tunnel test data. Subsequently, simulations of six different blockage ratios (BR = 0.8%, 2.5%, 5%, 7.8%, 10% and 15%) were carried out, and the results were compared comprehensively and analysed

detailedly to investigate the blockage effects on the pressure coefficients, aerodynamic forces and flow patterns around the tall building. Moreover, the same six BR cases under the uniform smooth inflow were simulated to explore the influence of flow properties on the blockage effects. Finally, some important conclusions can be summarized as follows:

- On the windward surface of the building, the blockage has a small influence on both $C_{p,mean}$ and $C_{p,rms}$; In contrast, on the lateral and leeward surfaces, both $C_{p,mean}$ and $C_{p,rms}$ increase significantly with the increase of BR.
 - Regarding the aerodynamic forces of the building under the turbulent inflow, as the BR increases from 0.8% to 15%, $C_{Fx,mean}$ increases significantly, mainly due to the increase in the suction on the leeward surface, whereas the wind force on the windward surface has a small negative contribution. In addition, both $C_{Fx,rms}$ and $C_{Fy,rms}$ increase monotonically with the increasing BR, while the latter is more significantly affected by the blockage. Affected by the blockage, the vortex shedding on the side surfaces of the model is enhanced, and the corresponding Strouhal number increases significantly.
 - Regarding the time-averaged flow fields, the increases of BR leads to the contraction of the recirculation region behind the building and the vortex to moves closer to the leeward surface of the building, which corresponding to the more negative pressure on the lateral and leeward surfaces and the higher drag force.
 - The increase of the BR leads to a thinner shear layer near the lateral sides of the building and higher velocity at the outer boundary of the shear layer. As a result, the blockage speeds up the formation and shedding of the vortex, resulting in the increases of Strouhal number. In addition, with the increase of BR, the intensity of the vortex increases and the interaction between the shear layer and the surfaces of the building is enhanced. Moreover, the coherence of the turbulent structures at the separation region and wake region increases obviously. These effects cause larger pressure fluctuations on the surfaces of the building which in turn impose larger overall wind loads upon the building.
 - The comparison of the results between the cases under the turbulent inflow and those under the uniform smooth inflow shows that the blockage effects of the latter is much stronger than those of the former. This phenomenon can be possibly explained as that the periodicity and integrity of vortex shedding are more evident, and the separated shear flow and wake flow from the model under the smooth inflow are wider than those under the turbulent inflow. These features are more susceptible to blockage. In other words, the blockage effects are weakened due to the enhancement of the fluctuation characteristics in the turbulent inflow.
 - According to the results, the blockage effects on the wind loads and flow field are negligible when the BR at 2.5%, while the blockage effects are obvious when the BR increases to 5%. In order to avoid the artificial acceleration of the flow due to the contraction by the computation boundaries, the value of the BR is suggested to be less than 3%.
- In summary, it must be noted that the blockage has a

huge impact on the wind loads and flow field of high-rise buildings. To the best knowledge of the authors, the mechanisms that relate the blockage to the induced effects on the buildings have not developed sufficiently. Not only can the approach flow affect the mechanisms of the blockage effects, but the flow patterns generated around the buildings are complicated and changes dramatically due to the variations in the structure shape. Thus, more attention should be paid to this issue. A large number of wind tunnel tests and CFD simulations need to be conducted on the blockage effects to explore the mechanisms. After carefully analyzing and fitting the data, more general conclusions, reasonable suggestions and applicable correction methods can be obtained.

Acknowledgments

The authors are very grateful for the support provided by the National Natural Science Foundation of China (90715040 and 91215302) and State Key Laboratory of Disaster Reduction in Civil Engineering, PR China (SLDRCE19-A-05). The authors would like to thank the Shanghai Supercomputer center for providing the computational resources for this study.

References

- AIJ. (2004). "Recommendations for loads on buildings", Architectural Institution of Japan, Tokyo, Japan.
- Awbi, H.B. (1983), "Effect of blockage on the Strouhal number of two-dimensional bluff bodies", *J. Wind Eng. Ind. Aerod.*, **12**(3), 353-362. [https://doi.org/10.1016/0167-6105\(83\)90055-7](https://doi.org/10.1016/0167-6105(83)90055-7).
- Blocken, B. (2014), "50 years of Computational Wind Engineering: Past, present and future", *J. Wind Eng. Ind. Aerod.*, **129**, 69-102. <https://doi.org/10.1016/j.jweia.2014.03.008>.
- Blocken, B. (2015), "Computational Fluid Dynamics for urban physics: Importance, scales, possibilities, limitations and ten tips and tricks towards accurate and reliable simulations", *Build. Environ.*, **91**, 219-245. <https://doi.org/10.1016/j.buildenv.2015.02.015>.
- Braun, A.L. and Awruch, A.M. (2009), "Aerodynamic and aeroelastic analyses on the CAARC standard tall building model using numerical simulation", *Comput. Struct.*, **87**(9), 564-581. <https://doi.org/10.1016/j.compstruc.2009.02.002>.
- Bruno, L., Fransos, D., Coste, N. and Bosco, A. (2010), "3D flow around a rectangular cylinder: A computational study", *J. Wind Eng. Ind. Aerod.*, **98**(6-7), 263-276. <http://dx.doi.org/10.1016/j.jweia.2009.10.005>.
- Bruno, L., Salvetti, M.V. and Ricciardelli, F. (2014), "Benchmark on the aerodynamics of a rectangular 5:1 Cylinder: An overview after the first four years of activity", *J. Wind Eng. Ind. Aerod.*, **126**, 87-106. <https://doi.org/10.1016/j.jweia.2014.01.005>.
- Cermak, J.E. (2003), "Wind-tunnel development and trends in applications to civil engineering", *J. Wind Eng. Ind. Aerod.*, **91**(3), 355-370. [http://dx.doi.org/10.1016/S0167-6105\(02\)00396-3](http://dx.doi.org/10.1016/S0167-6105(02)00396-3).
- Cochran, L. and Derickson, R. (2011), "A physical modeler's view of Computational Wind Engineering", *J. Wind Eng. Ind. Aerod.*, **99**(4), 139-153. <https://doi.org/10.1016/j.jweia.2011.01.015>.
- Courchesne, J. and Laneville, A. (1979), "A comparison of correction methods used in the evaluation of drag coefficient

- measurements for two-dimensional rectangular cylinders”, *J. Fluids Eng.*, **101**(4), 506-510. <https://doi.org/10.1115/1.3449019>.
- Courchesne, J. and Laneville, A. (1982), “An experimental evaluation of drag coefficient for rectangular cylinders exposed to grid turbulence”, *J. Fluids Eng.*, **104**(4), 523-527. <https://doi.org/10.1115/1.3241897>.
- Dagnew, A.K. and Bitsuamlak, G.T. (2013), “Computational evaluation of wind loads on buildings: a review”, *Wind Struct.*, **16**(6), 629-660. <http://dx.doi.org/10.12989/was.2013.16.6.629>.
- Dagnew, A.K. and Bitsuamlak, G.T. (2014), “Computational evaluation of wind loads on a standard tall building using LES”, *Wind Struct.*, **18**(5), 567-598. <http://dx.doi.org/10.12989/was.2014.18.5.567>.
- Davis, R.W., Moore, E.F. and Purtell, L.P. (1984), “A numerical-experimental study of confined flow around rectangular cylinders”, *Phys. Fluids.*, **27**(1), 46-59. <https://doi.org/10.1063/1.864486>.
- ESDU 85020 (2001), “Characteristics of atmospheric turbulence near the ground-Part II Single point data for strong winds (neutral atmosphere)”, Engineering Sciences Data Unit, IHS Inc., London, U.K., Report No. ESDU, 85020. pp.1-12
- Feng, C., Gu, M. and Zheng, D. (2019), “Numerical simulation of wind effects on super high-rise buildings considering wind veering with height based on CFD”, *J. Fluids Struct.*, **91** 102715. <https://doi.org/10.1016/j.jfluidstructs.2019.102715>.
- Fluent, A. (2011), “ANSYS Fluent Theory Guide 14.0”, ANSYS, Canonsburg, U.S.A.
- Franke, J., Hellsten, A., Schlünzen, H. and Carissimo, B. (2007), “Best practice guideline for the CFD simulation of flows in the urban environment: COST action 732 quality assurance and improvement of microscale meteorological models”, Meteorological Inst.
- Gao, Y., Gu, M. and Quan, Y. (2017). “Large eddy simulations of blockage ratio effect on a square cylinder in a uniform flow”, *The 9th Asia-Pacific Conference on Wind Engineering*, Auckland, New Zealand.
- Germano, M., Piomelli, U., Moin, P. and Cabot, W.H. (1991), “A dynamic subgrid-scale eddy viscosity model”, *Phys. Fluids Fluid Dyn.*, **3**(3), 1760-1765. <https://doi.org/10.1063/1.857955>.
- Hackett, J. and Cooper, K. (2001), “Extensions to Maskell’s theory for blockage effects on bluff bodies in a closed wind tunnel”, *Aeronaut. J.*, **105**(1050), 409-418. <https://doi.org/10.1017/S0001924000012380>.
- Huang, S., Li, Q. and Xu, S. (2007), “Numerical evaluation of wind effects on a tall steel building by CFD”, *J. Construct. Steel Res.*, **63**(5), 612-627. <https://doi.org/10.1016/j.jcsr.2006.06.033>.
- Huang, S.H., Li, Q.S. and Wu, J.R. (2010), “A general inflow turbulence generator for large eddy simulation”, *J. Wind Eng. Ind. Aerod.*, **98**(10-11), 600-617. <http://dx.doi.org/10.1016/j.jweia.2010.06.002>.
- Hunt, J.C., Wray, A.A. and Moin, P. (1988), “Eddies stream and convergence zones in turbulent flows”, Report No. CTR-S88, Center for Turbulence Research, Stanford, U.S.A.
- Irwin, P.A. (2009), “Wind engineering challenges of the new generation of super-tall buildings”, *J. Wind Eng. Ind. Aerod.*, **97**(7), 328-334. <https://doi.org/10.1016/j.jweia.2009.05.001>.
- Kim, D.H., Yang, K.S. and Senda, M. (2004), “Large eddy simulation of turbulent flow past a square cylinder confined in a channel”, *Comput. Fluids*, **33**(1), 81-96. [http://dx.doi.org/10.1016/S0045-7930\(03\)00040-9](http://dx.doi.org/10.1016/S0045-7930(03)00040-9).
- Laneville, A. (1990), “Turbulence and blockage effects on two dimensional rectangular cylinders”, *J. Wind Eng. Ind. Aerod.*, **33**(1), 11-20. [https://doi.org/10.1016/0167-6105\(90\)90016-6](https://doi.org/10.1016/0167-6105(90)90016-6).
- Li, Q.S. and Melbourne, W.H. (1995), “An experimental investigation of the effects of free-stream turbulence on streamwise surface pressures in separated and reattaching flows”, *J. Wind Eng. Ind. Aerod.*, **54-55** 313-323. [https://doi.org/10.1016/0167-6105\(94\)00050-N](https://doi.org/10.1016/0167-6105(94)00050-N).
- Martinuzzi, R. and Tropea, C. (1993), “The flow around surface-mounted, prismatic obstacles placed in a fully developed channel flow (data bank contribution)”, *J. Fluids Eng.*, **115**(1), 85-92. <https://doi.org/10.1115/1.2910118>.
- Maskell, E.C. (1963), “A theory of the blockage effects on bluff bodies and stalled wings in a closed wind tunnel”, Aeronautical Research Council Reports and Memoranda, London.
- Murakami, S. (1998), “Overview of turbulence models applied in CWE-1997”, *J. Wind Eng. Ind. Aerod.*, **74**, 1-24. [https://doi.org/10.1016/S0167-6105\(98\)00004-X](https://doi.org/10.1016/S0167-6105(98)00004-X).
- Nakagawa, S., Nitta, K. and Senda, M. (1999), “An experimental study on unsteady turbulent near wake of a rectangular cylinder in channel flow”, *Experim. Fluids.*, **27**(3), 284-294. <https://doi.org/10.1007/s003480050>.
- Okajima, A., Yi, D., Kimura, S. and Kiwata, T. (1997), “The blockage effects for an oscillating rectangular cylinder at moderate Reynolds number”, *J. Wind Eng. Ind. Aerod.*, **69**, 997-1011. [https://doi.org/10.1016/S0167-6105\(97\)00223-7](https://doi.org/10.1016/S0167-6105(97)00223-7).
- Okajima, A., Yi, D., Sakuda, A. and Nakano, T. (1997), “Numerical study of blockage effects on aerodynamic characteristics of an oscillating rectangular cylinder”, *J. Wind Eng. Ind. Aerod.*, **67-68**(4), 91-102. [https://doi.org/10.1016/S0167-6105\(97\)00065-2](https://doi.org/10.1016/S0167-6105(97)00065-2).
- Patruno, L. and Ricci, M. (2017), “On the generation of synthetic divergence-free homogeneous anisotropic turbulence”, *Comput. Meth. Appl. Mech. Eng.*, **315**, 396-417. <https://doi.org/10.1016/j.cma.2016.11.005>.
- Petty, D. (1979), “The effect of turbulence intensity and scale on the flow past square prisms”, *J. Wind Eng. Ind. Aerod.*, **4**(3), 247-252. [https://doi.org/10.1016/0167-6105\(79\)90005-9](https://doi.org/10.1016/0167-6105(79)90005-9).
- Raju, K.R. and Singh, V. (1975), “Blockage effects on drag of sharp-edged bodies”, *J. Wind Eng. Ind. Aerod.*, **1**(3), 301-309. [https://doi.org/10.1016/0167-6105\(75\)90023-9](https://doi.org/10.1016/0167-6105(75)90023-9).
- Ramamurthy, A., Balachandar, R. and Vo, D.N. (1989), “Blockage correction for sharp-edged bluff bodies”, *J. Eng. Mech.*, **115**(7), 1569-1576. [https://doi.org/10.1061/\(ASCE\)0733-9399\(1989\)115:7\(1569\)](https://doi.org/10.1061/(ASCE)0733-9399(1989)115:7(1569)).
- Reyes, M., Velazquez, A., Martin, E. and Arias, J.R. (2013), “Experimental study on the confined 3D laminar flow past a square prism with a high blockage ratio”, *Int. J. Heat Fluid Flow.*, **44**, 444-457. <https://doi.org/10.1016/j.ijheatfluidflow.2013.08.001>.
- Ricci, M., Patruno, L., Kalkman, I., de Miranda, S. and Blocken, B. (2018), “Towards LES as a design tool: Wind loads assessment on a high-rise building”, *J. Wind Eng. Ind. Aerod.*, **180**, 1-18. <https://doi.org/10.1016/j.jweia.2018.07.009>.
- Schlichting, H. and Gersten, K. (2016), “Boundary-layer theory”, Springer-Verlag, Berlin, Germany.
- Smirnov, A., Shi, S. and Celik, I. (2001), “Random flow generation technique for large eddy simulations and particle-dynamics modeling”, *J. Fluids Eng.*, **123**(2), <https://doi.org/10.1115/1.1369598>.
- Tamura, T. (2008), “Towards practical use of LES in wind engineering”, *J. Wind Eng. Ind. Aerod.*, **96**(10), 1451-1471. <https://doi.org/10.1016/j.jweia.2008.02.034>.
- Thordal, M.S., Bennetsen, J.C. and Koss, H.H.H. (2019), “Review for practical application of CFD for the determination of wind load on high-rise buildings”, *J. Wind Eng. Ind. Aerody.*, **186** 155-168. <https://doi.org/10.1016/j.jweia.2018.12.019>.
- Tominaga, Y., Mochida, A., Yoshie, R., Kataoka, H., Nozu, T., Yoshikawa, M. and Shirasawa, T. (2008), “AIJ guidelines for practical applications of CFD to pedestrian wind environment around buildings”, *J. Wind Engineering Ind. Aerod.*, **96**(10), 1749-1761. <https://doi.org/10.1016/j.jweia.2008.02.058>.
- Utsunomiya, H., Nagao, F., Ueno, Y. and Noda, M. (1993), “Basic study of blockage effects on bluff bodies”, *J. Wind Eng. Ind.*

- Aerod.*, **49**(1), 247-256. [https://doi.org/10.1016/0167-6105\(93\)90020-O](https://doi.org/10.1016/0167-6105(93)90020-O).
- Wijesooriya, K., Mohotti, D., Chauhan, K. and Dias-da-Costa, D. (2019), "Numerical investigation of scale resolved turbulence models (LES, ELES and DDES) in the assessment of wind effects on supertall structures", *J. Build. Eng.*, **25**. <https://doi.org/10.1016/j.jobee.2019.100842>.
- Xie, Z.T. and Castro, I.P. (2008), "Efficient generation of inflow conditions for large eddy simulation of street-scale flows", *Flow, Turbul. Combust.*, **81**(3), 449-470. <https://doi.org/10.1007/s10494-008-9151-5>.
- Yan, B. and Li, Q. (2015), "Inflow turbulence generation methods with large eddy simulation for wind effects on tall buildings", *Comput. Fluids*, **116**, 158-175. <https://doi.org/10.1016/j.compfluid.2015.04.020>.
- Yu, Y., Yang, Y. and Xie, Z. (2018), "A new inflow turbulence generator for large eddy simulation evaluation of wind effects on a standard high-rise building", *Build. Environ.*, **138**, 300-313. <https://doi.org/10.1016/j.buildenv.2018.03.059>.
- Zhang, Y., Habashi, W.G. and Khurram, R.A. (2015), "Predicting wind-induced vibrations of high-rise buildings using unsteady CFD and modal analysis", *J. Wind Eng. Ind. Aerod.*, **136**, 165-179. <https://doi.org/10.1016/j.jweia.2014.11.008>.
- Zheng, D., Zhang, A. and Gu, M. (2012), "Improvement of inflow boundary condition in large eddy simulation of flow around tall building", *Eng. Appl. Comput. Fluid Mech.*, **6**(4), 633-647. <https://doi.org/10.1080/19942060.2012.11015448>.